Materials Advances

ROYAL SOCIETY OF CHEMISTRY

PAPER

View Article Online
View Journal | View Issue

Check for updates

Cite this: *Mater. Adv.*, 2025, **6**, 7332

A novel n–p–n type ZnO/BiOI/AgI ternary heterojunction with enhanced visible-light photocatalytic performance for pollutant degradation and antibacterial applications

Xinxin Li,[a] Lianjie Du,[a] Zhou Wan,[b] Doudou Xu*[c] and Chen Liu *[ad]

In this study, novel ZnO/BiOI/AgI ternary heterojunction photocatalysts were synthesized *via* a facile precipitation method to address challenges in organic pollutant degradation and microbial disinfection under visible light irradiation. The composites were systematically characterized (XRD, SEM, TEM, XPS, BET, UV-vis DRS, and PL), showing significantly enhanced visible light absorption, efficient charge carrier separation, and superior photocatalytic performance, compared to binary and single-component counterparts. The optimized ZnO/BiOI/AgI-3030 sample achieved 98.1% degradation of Rhodamine B (RhB) and 59.1% degradation of Norfloxacin (NOR) within 3 hours, attributed to the synergistic effects of the heterojunction structure, which facilitated efficient charge transfer and promoted the generation of reactive oxygen species (ROS). Furthermore, the composite demonstrated remarkable antibacterial activity against *Escherichia coli* (*E. coli*), *Staphylococcus aureus* (*S. aureus*), and *methicillin-resistant Staphylococcus aureus* (*MRSA*), with bactericidal rates exceeding 99.8%. Cytotoxicity assays revealed 88.79% inhibition of DLD-1 colorectal cancer cells. Mechanistic studies confirmed the formation of a unique n–p–n heterostructure, enabling effective charge carrier separation and strong redox capabilities. Additionally, the photocatalysts exhibited excellent stability and reusability over four consecutive degradation cycles, maintaining high catalytic efficiency. These findings underscore the potential of ZnO/BiOI/AgI ternary composites as efficient and sustainable photocatalysts for environmental remediation and antimicrobial applications.

Received 12th April 2025,
Accepted 16th August 2025

DOI: 10.1039/d5ma00354g

rsc.li/materials-advances

1. Introduction

The rapid pace of urbanization and industrialization has resulted in severe water pollution, affecting both surface water and groundwater worldwide. Organic pollutants, such as dyes and pharmaceuticals, are widely detected in aquatic environments and pose significant threats to the ecosystems, aquatic organisms and human health.[1,2] These pollutants are chemically stable and highly resistant to conventional treatment methods, leading to their persistent accumulation in the environment.[3,4] For instance, Rhodamine B (RhB), a synthetic dye extensively used in textile and printing industries, is carcinogenic, teratogenic and mutagenic. Its excessive presence in aquatic environments not only alters water coloration but also restricts surface water oxidation.[5–7] Similarly, pharmaceuticals, such as antibiotics, which are widely used and incompletely metabolized, are frequently discharged into aquatic environments.[8,9] For example, Norfloxacin (NOR), a quinolone antibiotic, is excreted with 40–90% of its active metabolites intact, posing serious risks to ecosytems and human health.[10,11] Therefore, the rapid and efficient removal of such pollutants from wastewater is critical for environmental protection and public health.

Photocatalysis has emerged as an advanced oxidation process (AOP) for wastewater treatment, disinfection and air purification, offering advantages such as high efficiency, environmental friendliness and cost-effectiveness, compared to conventional methods like ozone oxidation, adsorption and algal degradation.[12,13] During photocatalysis, photoactive semiconductors generate electron/hole (e^-/h^+) pairs under light illumination, which subsequently produce reactive oxygen species (ROS) to decompose organic pollutants.[14,15] For example, Cu(II)-based metal–organic frameworks (MOFs) have demonstrated

---

[a] *Department of Chemical Biology, School of Pharmaceutical Science, Capital Medical University, Beijing 100069, China. E-mail: cliu@ccmu.edu.cn*
[b] *Department of Beijing Anding Hospital, Capital Medical University, Beijing 100069, China*
[c] *Chongqing Pharmaceutical Science Technology School, Chongqing 400700, China. E-mail: xdd@cqpsts.cn*
[d] *Beijing Area Major Laboratory of Peptide and Small Molecular Drugs, Engineering Research Center of Endogenous Prophylactic of Ministry of Education of China, China*

impressive photocatalytic performance, exhibiting 99% degradation efficiency of RhB under visible light irradiation with the assistance of H_2O_2, which underscores the versatility of MOFs in organic pollutant removal.[16] However, the photocatalytic activity of semiconductors is influenced by factors such as light absorption efficiency, redox potential, and the separation rate of photogenerated carriers. To overcome these limitations, strategies including heterojunction construction, doping, single atom catalysis and defect engineering have been explored.[17] Among these, the construction of heterojunction structures has garnered particular attention due to the synergistic effect of multiple components, which broaden the visible light absorption range and improve carrier separation efficiency.[18–20] Notably, S-scheme heterojunctions have been shown to enhance charge transfer rates and suppress charge recombination, as evidenced by recent studies on ZnO-based systems with $CuBi_2O_4$, which demonstrated efficient degradation of antibiotics and dyes through photocatalytic activation of peroxymonosulfate.[21]

To date, metal oxide semiconductor-based nanomaterials (TiO_2, SnO_2, ZnO, Fe_2O_3, and WO_3) have been extensively explored for photocatalytic degradation of harmful organic pollutants.[22] Among these, zinc oxide (ZnO) has garnered significant attention as an important n-type semiconductor due to its direct band gap of 3.3 eV, high exciton binding energy, excellent electrochemical stability and low toxicity.[23–25] For instance, ZnO nanoparticles in various morphologies such as nanospheres, nanotubes and nanorods demonstrate promising photocatalytic performance, with ZnO nanospheres exhibiting a degradation efficiency of 98.64% for methylene blue and an effective degradation rate of 0.0112 min^{-1} for ofloxacin.[26] However, ZnO suffers from intrinsic limitations, including a narrow light absorption range confined to the ultraviolet spectrum and rapid recombination of photogenerated e^-/h^+ pairs, which significantly restrict its quantum efficiency.[27,28] To address these challenges, coupling ZnO with narrow bandgap semiconductors to form heterojunction structures has been proposed as an effective strategy. Heterojunctions not only facilitate efficient charge separation and suppress the recombination of e^-/h^+ pairs but also extend the light absorption range from the UV to the visible spectrum.[29]

Among various heterojunction systems, the combination of ZnO and bismuth oxyiodide (BiOI) has attracted particular attention. BiOI, a p-type semiconductor with a narrow bandgap (1.63–1.94 eV), has been widely studied as a promising photocatalyst due to its unique two-dimensional layered structure.[30] This structure facilitates internal electric field generation, which promotes the separation of photoinduced carriers.[31,32] For example, ZnO/BiOI nanorod heterostructures have been shown to degrade up to 79% of RhB dyes within 4 hours under visible light irradiation.[33] Other BiOI-based heterojunction materials, such as Bi_2O_3–BiOI and CeO_2–BiOI, have also demonstrated promising photocatalytic performance.[34,35] These findings highlight the potential of BiOI-based heterojunctions for the effective degradation of organic pollutants. However, the photocatalytic efficiency of ZnO/BiOI heterojunctions remains limited by the rapid recombination of photogenerated carriers.[36]

To enhance the photocatalytic performance and antibacterial effects of the composites, silver semiconductor materials have been introduced. Silver halides (AgX, X = Cl, Br, and I) are well-known for their strong photosensitivity, which facilitates the degradation of various organic compounds.[37] Additionally, silver semiconductors exhibit excellent antibacterial properties, making them highly effective antimicrobial agents.[38] Among them, silver iodide (AgI), an n-type semiconductor with a band gap of 2.8 eV, has attracted significant interest due to its suitable band structure. Its more negative conduction band potential compared to many other semiconductors enables efficient charge separation, enhanced reactive radical generation, and effective decomposition of various contaminants.[39,40] However, AgI suffers from severe photocorrosion and particle agglomeration, which limit its stability and practical applications.[41,42] To mitigate these issues, AgI is often composited with other materials. For example, binary AgI/ZnO composites have demonstrated a photodegradation rate of ciprofloxacin (CIP) of 0.0463 min^{-1} and photocatalytic production of H_2 of 2.725 mmol g^{-1} h^{-1}.[43] Nonetheless, simple composite structures do not always resolve the instability of AgI. For instance, the photocatalytic activity of ZnO/AgI for the degradation of MO was significantly reduced, retaining only 73.5% of its initial activity after the first run. Additionally, the composite material underwent a colour change from yellow to brown, indicating AgI decomposition.[44] To address these challenges, combining AgI with other semiconductors in a stable heterojunction structure has proven to be an effective strategy for improving both stability and photocatalytic efficiency.[45–47]

In this paper, novel ZnO/BiOI/AgI ternary heterojunction photocatalysts were synthesized *via* a precipitation method. By integrating the wide bandgap ZnO with narrow band gap semiconductors BiOI and AgI, it is aimed to enhance visible light driven photocatalytic activity and improve charge separation efficiency of the composite photocatalysts. The photocatalytic performance of ZnO/BiOI/AgI composites was evaluated using RhB and NOR as model pollutants. Additionally, their antibacterial activity and cytotoxicity were assessed. Based on the experimental results and free radical assay, a photocatalytic mechanism was proposed. This work suggests that ZnO/BiOI/AgI photocatalysts may be effective for the development of efficient photocatalysts for the degradation of organic pollutants and antimicrobial applications.

2. Materials and methods

2.1. Synthesis of composites

ZnO nanomaterials were synthesized using a precipitation method. Initially, 200 mL of 0.3 mol L^{-1} sodium hydroxide (NaOH, Macklin) solution was prepared. Subsequently, 0.02 mol of zinc nitrate hexahydrate ($Zn(NO_3)_2 \cdot 6H_2O$, Sinopharm Chemical Reagent) was slowly added to the alkaline solution under continuous stirring at room temperature for 10 minutes. The molar ratio of OH^- to Zn^{2+} in the reaction was maintained at 3 : 1. The mixture was then heated to 80 °C and kept under these conditions for 3 hours. After cooling to room temperature, the resulting white precipitate was collected by centrifugation, thoroughly washed with distilled water and ethanol, and dried in a vacuum oven for 24 hours to obtain ZnO particles.

A series of ZnO/BiOI composites with varying BiOI contents were synthesized and labeled as ZnO/BiOI-*x*, where *x* represents the weight percentage of BiOI. For example, to synthesize ZnO/BiOI-30 (indicates 30 wt% BiOI), 0.300 g of the previously prepared ZnO was dispersed in 100 mL distilled water by ultrasonic treatment for 10 minutes. To achieve the desired BiOI content of 30 wt%, 0.177 g of bismuth nitrate pentahydrate ($Bi(NO_3)_3{\cdot}5H_2O$, Aladdin) was added to the dispersion, as this corresponds to the stoichiometric amount required to form 0.129 g of BiOI, as shown in Table S1 in the SI. The mixture was stirred for 1 hour to ensure uniform distribution. Subsequently, 30 mL of potassium iodide (KI, Macklin) aqueous solution was added dropwise, followed by a reaction at 96 °C for 3 hours. The resulting suspension was centrifuged, and the precipitate was washed twice with distilled water and ethanol. The final product was dried in a vacuum oven at room temperature for 24 hours.

ZnO/AgI nanocomposites were synthesized by substituting $Bi(NO_3)_3{\cdot}5H_2O$ with silver nitrate ($AgNO_3$, Sinopharm Chemical Reagent) in the reaction process. The weight percentage of AgI was kept at 30%. The calculation for determining the required amount of $AgNO_3$ to achieve the desired AgI content was performed in a similar manner to the method used for ZnO/BiOI synthesis.

For the synthesis of ZnO/BiOI/AgI ternary nanocomposites, a series of composite materials with varying AgI contents were synthesized and labeled as ZnO/BiOI/AgI-*xy*, where *x* and *y* represent the weight percentages of BiOI and AgI, respectively. For instance, ZnO/BiOI/AgI-3030 (3030 indicates 30 wt% BiOI and 30 wt% AgI) was prepared by dispersing 0.300 g of ZnO in 100 mL of distilled water using ultrasonic treatment for 10 minutes. Subsequently, 0.177 g of $Bi(NO_3)_3{\cdot}5H_2O$ and 0.133 g of $AgNO_3$ were added to the dispersion, and the mixture was stirred in the dark for 1 hour to ensure complete dispersion. Then, 30 mL of KI aqueous solution was added dropwise and the reaction was conducted at 96 °C for 3 hours. Table S2 summarizing the specific ratios for ZnO/BiOI/AgI-*xy* is provided in the SI. The resulting precipitate was centrifuged, washed thoroughly with distilled water and ethanol, and dried in a vacuum oven at room temperature for 24 hours. A schematic representation of the ZnO/BiOI/AgI synthesis process is shown in Scheme 1.

2.2. Material characterization

All samples underwent comprehensive characterization. The Hitachi 4800 field emission scanning electron microscope (SEM, Japan) and the JEM-2100 instrumental transmission electron microscope (TEM, Japan) were used to observe the surface morphology of the synthesized samples. The JEM-2100F (Japan) was used to record high-resolution electron microscopy (HRTEM) images to further understand the crystal structure. The Bruker D8 Advance X-ray diffractometer (XRD, Germany) was used to characterize the crystalline phases of the synthetic materials. The Energy dispersive X-ray spectrometer (EDS) was used to examine elemental compositions for elemental mapping. The ESCALAB 250 X-ray photoelectron spectrometer (XPS, USA) was used to analyze the surface chemistry. The Quantachrome Autosorb iQ analyzer (USA) was used to measure N_2 adsorption–desorption isotherms for pore size analysis of the synthesized samples. The Agilent Cary 5000 UV-Vis-NIR UV-Vis diffuse reflectance spectrometer (UV-Vis DRS, USA) was used to characterize the optical properties of the samples. The Chenhua CHI660E series electrochemical analyser (China) was used to measure the transient photocurrent response (TPC) and electrochemical impedance spectroscopy (EIS) was used to analyse the photogenerated carrier separation. The FLS1000 photoluminescence spectrometer (UK) was used to collect photoluminescence (PL) spectra to assess photogenerated carrier recombination rates. The JES-FA200 electron paramagnetic resonance spectrometer (Japan) was used to detect electron spin resonance (ESR) signals of free radicals. The Agilent 6490 Series triple quadrupole liquid chromatography–mass spectrometry system (LC–MS, USA) was used for the detection of RhB degradation intermediates to probe the degradation process of the contaminants.

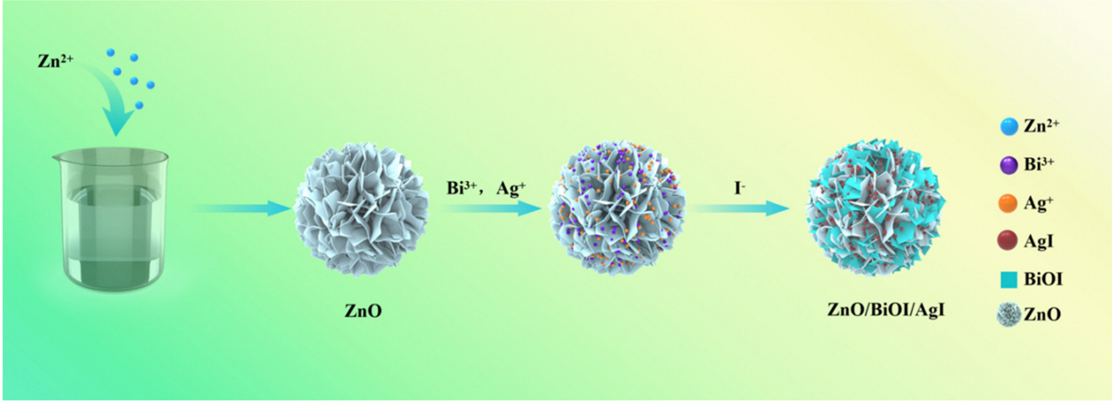

Scheme 1 Preparation process of ZnO/BiOI/AgI nanocomposites.

2.3. Photocatalytic performance

The photocatalytic performance of the synthesized catalysts was assessed by testing their ability to degrade organic pollutants, specifically Rhodamine B (RhB, Macklin) as a representative dye and Norfloxacin (NOR, Macklin) as a model antibiotic under visible light irradiation. A 300 W Xe lamp equipped with a 420 nm cut-off filter served as the visible light source. For a typical degradation experiment, 50 mg of photocatalysts was suspended in 50 mL of an aqueous solution containing 10 mg L^{-1} of RhB or NOR. The suspension was stirred in the absence of light for 60 minutes to establish adsorption–desorption equilibrium between the photocatalysts and the pollutants. Afterward, the photocatalytic reaction was initiated by exposing the system to visible light, with the reaction temperature maintained at room temperature using water circulation. At 30-minute intervals, 3 mL of the reaction mixture was withdrawn, filtered through a 0.22 μm membrane, and analyzed. The concentrations of RhB and NOR were determined using a UV-visible spectrophotometer (Shimadzu UV-2600, Japan) by monitoring their respective absorption peaks at 553 nm and 272 nm.[48,49]

The reusability and stability of ternary ZnO/BiOI/AgI nanocomposites were investigated through cyclic photocatalytic degradation experiments using RhB and NOR as model pollutants. The ZnO/BiOI/AgI-3030 sample was chosen for these tests. Following each degradation cycle, the photocatalysts were recovered *via* centrifugation, washed thoroughly with deionized water and ethanol, and then dried overnight at room temperature. The recovered photocatalysts were reused for four successive cycles to evaluate their long-term stability and reusability.

To identify the active species involved in the photocatalytic degradation, radical trapping experiments were conducted using 1 mM scavengers. Benzoquinone (BQ, Aladdin) was employed to capture superoxide anion radicals ($^{\bullet}O_2^{-}$), 2-propanol (IPA, Aladdin) was used to quench hydroxyl radicals ($^{\bullet}OH$) and ammonium oxalate (AO, Aladdin) was added to trap photogenerated holes (h^{+}). The degradation efficiencies were compared to determine the contribution of each reactive species to the photocatalytic mechanism.

2.4. Antibacterial performance

The antibacterial activity of ZnO, ZnO/BiOI, ZnO/AgI and ZnO/BiOI/AgI composites was tested against three bacterial models: *Escherichia coli* (*E. coli*, ATCC 8739) representing Gram-negative (G^{-}) bacteria, *Staphylococcus aureus* (*S. aureus*, ATCC 6538) representing Gram-positive (G^{+}) bacteria, and *methicillin-resistant Staphylococcus aureus* (*MRSA*, ATCC 43300) as a drug-resistant bacterial strain. ZnO/BiOI composites with 30 wt% BiOI (denoted as BiOI-30) and ZnO/AgI composites with 30 wt% AgI (denoted as AgI-30) were selected as typical samples for comparison. For the ZnO/BiOI/AgI composites, BiOI-30 was used as the baseline, while the AgI content was varied from 10 wt% to 40 wt%. All glassware and bacterial cultures used in the experiments were autoclaved to ensure sterility. The bacterial cells were grown in trypticase soy liquid medium (TSB, AOBOX).

The bacteriostatic activity of the photocatalysts was assessed using the agar well diffusion method. Bacterial suspensions were prepared and adjusted to a concentration of 10^7 CFU per mL. A sterile cotton swab was used to evenly spread the bacterial solution across the surface of agar plates. Wells with a diameter of 6 mm were created using a sterile borer. For sample preparation, 20 mg of the photocatalyst was dispersed in 2 mL of phosphate buffer solution (PBS) and irradiated under a 300 W Xe lamp with a 420 nm cut-off filter for 60 minutes. After irradiation, 40 μL of the photocatalyst suspension was introduced into each well, and the plates were incubated upside down at 37 °C for 24 hours. Wells without photocatalyst served as blank controls. The antibacterial performance was quantified by measuring the diameter of the inhibition zones formed around the wells.

In addition to the inhibition zone measurements, the reduction in bacterial concentration during the photocatalytic antibacterial process was evaluated using the plate count method. A 2 mL bacterial suspension (*E. coli*, *S. aureus*, or *MRSA*) was mixed with 18 mL of PBS, and the bacterial concentration was adjusted to 10^6 CFU per mL. Subsequently, 20 mg of the photocatalyst was added to the mixture, which was then exposed to visible light irradiation for 60 minutes. A blank control group without photocatalyst powder was also included. At 20-minute intervals, 100 μL of the suspension was withdrawn, serially diluted, and spread on an agar plate. After incubation at 37 °C for 24 hours, bacterial colonies were counted to determine the concentration of surviving bacteria. Six parallel experiments were conducted for each sample to ensure accuracy and reproducibility of the results.

2.5. Cytotoxicity performance

The cytotoxic effects of photocatalytic composites on colorectal cancer cells (DLD-1 cells, obtained from Chongqing Institute for Food and Drug Control) were assessed using a CCK-8 assay. Briefly, DLD-1 cells (5000 cells per well) were seeded into 96-well plates and cultured overnight at 37 °C in a 5% CO_2 incubator to allow cell attachment. Photocatalytic composites at various concentrations (0–250 μg mL^{-1}) were prepared in a complete medium (CM: RPMI1640 contains 10% FBS, Bioyotime Technology, Beijing, China) and pre-activated under a 300 W Xe lamp to trigger their photocatalytic activity. Following this, the CM in each well was replaced with 100 μL of the photocatalytic nanocomposite solution, and the cells were incubated for an additional 24 hours.

For the CCK-8 assay, the photocatalytic nanocomposite solutions were removed from the wells, and the cells were gently washed twice with 100 μL of pre-warmed CM. Subsequently, 90 μL of fresh CM and 10 μL CCK-8 solution (Tongren Institute of Chemical Research, Japan) were carefully added to each well, ensuring that no air bubbles were present, as they could interfere with the reaction. The plates were then incubated at 37 °C for 4 hours. The absorbance at 450 nm was recorded using a microplate reader (Varioskan Flash, Thermo Scientific, USA). Three independent experiments were conducted, each with triplicate samples to ensure reproducibility and reliability of the results.

3. Results and discussion

3.1. Characterization of the photocatalysts

3.1.1. Surface morphology observation. The surface morphology and structure of ZnO, ZnO/BiOI, ZnO/AgI and ZnO/BiOI/AgI nanocomposites were investigated using SEM. As depicted in Fig. 1a, the pure ZnO sample exhibits a flower-like structure with a diameter of approximately 1 μm. This configuration is formed by the aggregation of numerous nanosheets, which converge at the center to create a three-dimensional flower-like morphology. In Fig. 1b, the ZnO/BiOI samples reveal the presence of regular square BiOI nanosheets interspersed among ZnO nanosheets. Fig. 1c illustrates that small spherical AgI particles are adhered to the surface of ZnO nanosheets. The SEM image in Fig. 1d demonstrates that the ZnO/BiOI/AgI composite retains the flower-like structure, with both square BiOI nanosheets and spherical AgI particles deposited on the ZnO nanosheets, indicating the successful synthesis of the composite material.

The microstructure of the ZnO/BiOI/AgI was characterized using TEM and HRTEM. In Fig. 2a, the TEM image of ZnO sample reveals a flower-like structure composed of nanosheets. Regions with a higher density of nanosheets appear opaque, while the edges with fewer nanosheets are more transparent. Fig. 2b illustrates the ZnO/BiOI/AgI sample, which exhibits a more opaque edge compared to the ZnO image. This increased opacity is due to the deposition of BiOI and AgI on ZnO, which aligns with the SEM image results.[50] Fig. 2c shows the HRTEM image of the ZnO/BiOI/AgI nanocomposite with distinct fringe spacings. Three lattice fringes are observed with spacings of 0.260, 0.166 and 0.230 nm, corresponding to the (002) plane of ZnO, the (212) plane of BiOI and the (110) plane of AgI, respectively. These measurements further confirm the presence of ZnO, BiOI and AgI in the ZnO/BiOI/AgI photocatalyst.

3.1.2. Physical analysis. XRD analysis was used to elucidate the crystal structures and phase compositions of the photocatalysts, with the results presented in Fig. 3. The patterns align well with reference peaks reported from standard cards. All photocatalyst samples exhibit ZnO in a hexagonal wurtzite phase structure (JCPDS no. 99-0111), with peaks at 31.77°, 34.42°, 36.25°, 47.54°, 56.59°, 62.85°, 66.37°, 67.94° and 69.08°, corresponding to the (100), (002), (101), (102), (110), (103), (200), (112) and (201) planes.[51] For ZnO/BiOI samples, additional diffraction peaks indicate the lattice planes of the standard tetragonal structure of BiOI (JCPDS no. 10-0445), with peaks at 24.29°, 29.65°, 31.66°, 45.38°, 49.81°, 55.15°, and 66.12°, attributed to the (101), (102), (110), (200), (005), (212) and (220) planes.[52] For the ZnO/BiOI/AgI samples, peaks at 22.32°, 23.71°, 25.35°, 39.20°, 42.63°, 46.31°, and 71.04° associated with the (100), (002), (101), (110), (103), (112) and (300) planes corresponding to the hexagonal structure of AgI (JCPDS no. 09-0374) were also observed.[53] Notably, the characteristic peaks of ZnO, BiOI and AgI were all detected in ZnO/BiOI/AgI samples, indicating that the incorporation of BiOI and AgI into ZnO does not significantly alter the crystal structure of ZnO. These XRD results confirm the successful synthesis of the ternary ZnO/BiOI/AgI composite.

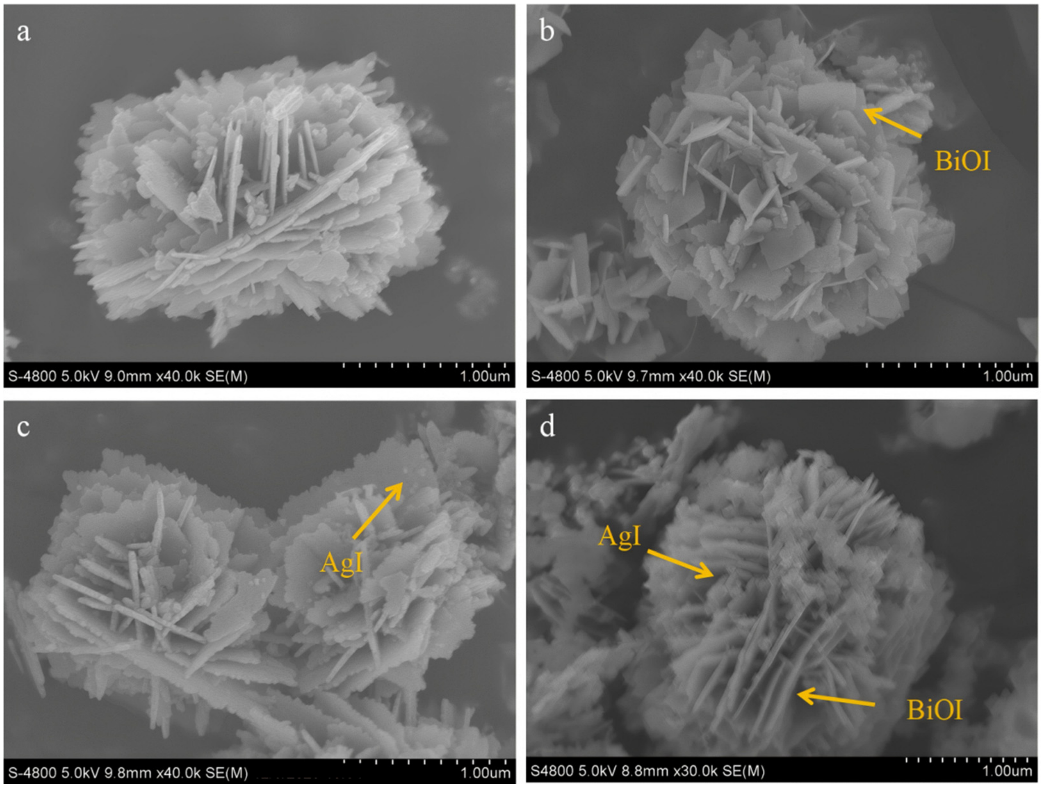

Fig. 1 The SEM images of (a) ZnO, (b) ZnO/BiOI, (c) ZnO/AgI and (d) ZnO/BiOI/AgI.

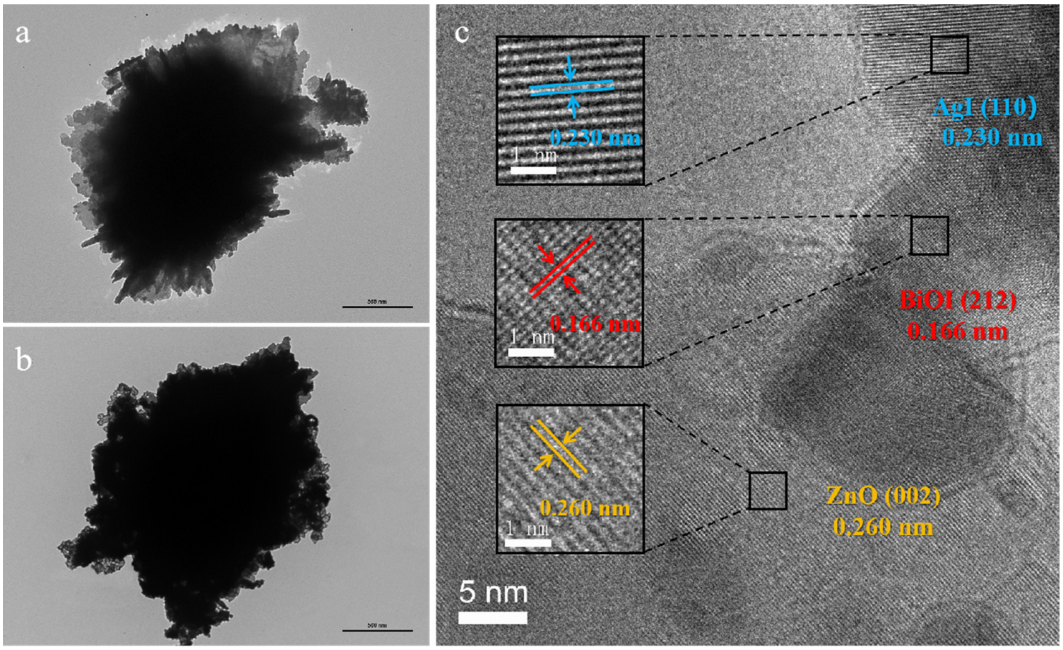

Fig. 2 The TEM images of (a) ZnO and (b) ZnO/BiOI/AgI. (c) HRTEM image of ZnO/BiOI/AgI.

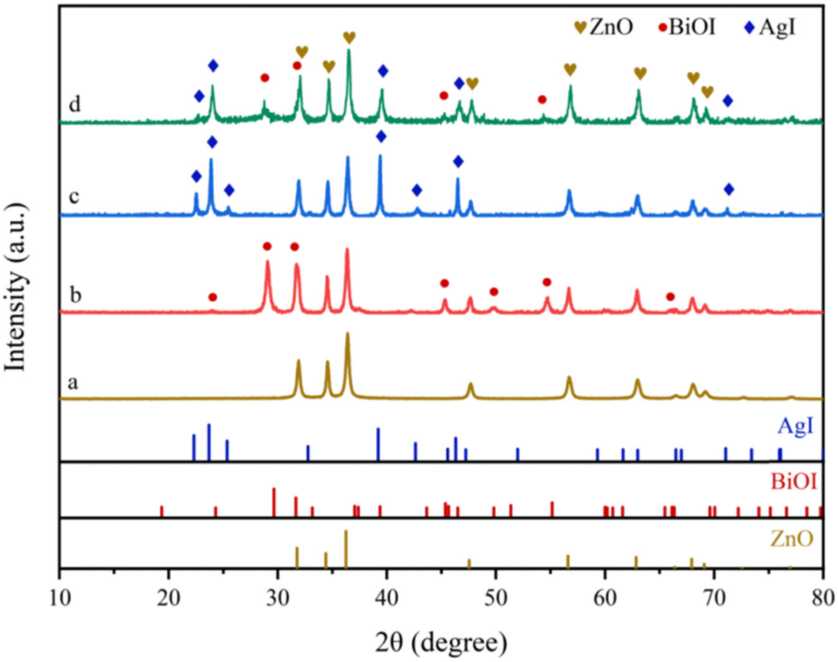

Fig. 3 XRD patterns of ZnO/BiOI/AgI. (a) ZnO, (b) ZnO/BiOI, (c) ZnO/AgI and (d) ZnO/BiOI/AgI.

3.1.3. **Surface elemental analysis.** Fig. 4 presents the XPS analysis results of the ZnO/BiOI/AgI photocatalysts, examining the elemental composition and chemical states. The spectra are calibrated using the C 1s peak at 284.6 eV. The survey spectrum (Fig. 4a) confirms the presence of Zn, Bi, Ag, I and O in the composite. In the Zn 2p spectrum (Fig. 4b), peaks at 1022.3 and 1045.2 eV correspond to Zn $2p_{3/2}$ and Zn $2p_{1/2}$, respectively,[54,55] indicating that Zn is in a divalent oxidation state. The Bi 4f spectrum (Fig. 4c) shows the peaks at 159.0 and 164.5 eV, attributed to Bi $4f_{7/2}$ and Bi $4f_{5/2}$, implying the presence of Bi^{3+} in the composite.[56,57] In the Ag 3d spectrum (Fig. 4d), the peaks at 368.3 and 374.4 eV are assigned to Ag $3d_{5/2}$ and Ag $3d_{3/2}$.[45] These peaks are attributed to AgI, indicating the valence state of Ag^{+}. No metallic silver peak is observed (two peaks at 367.2 and

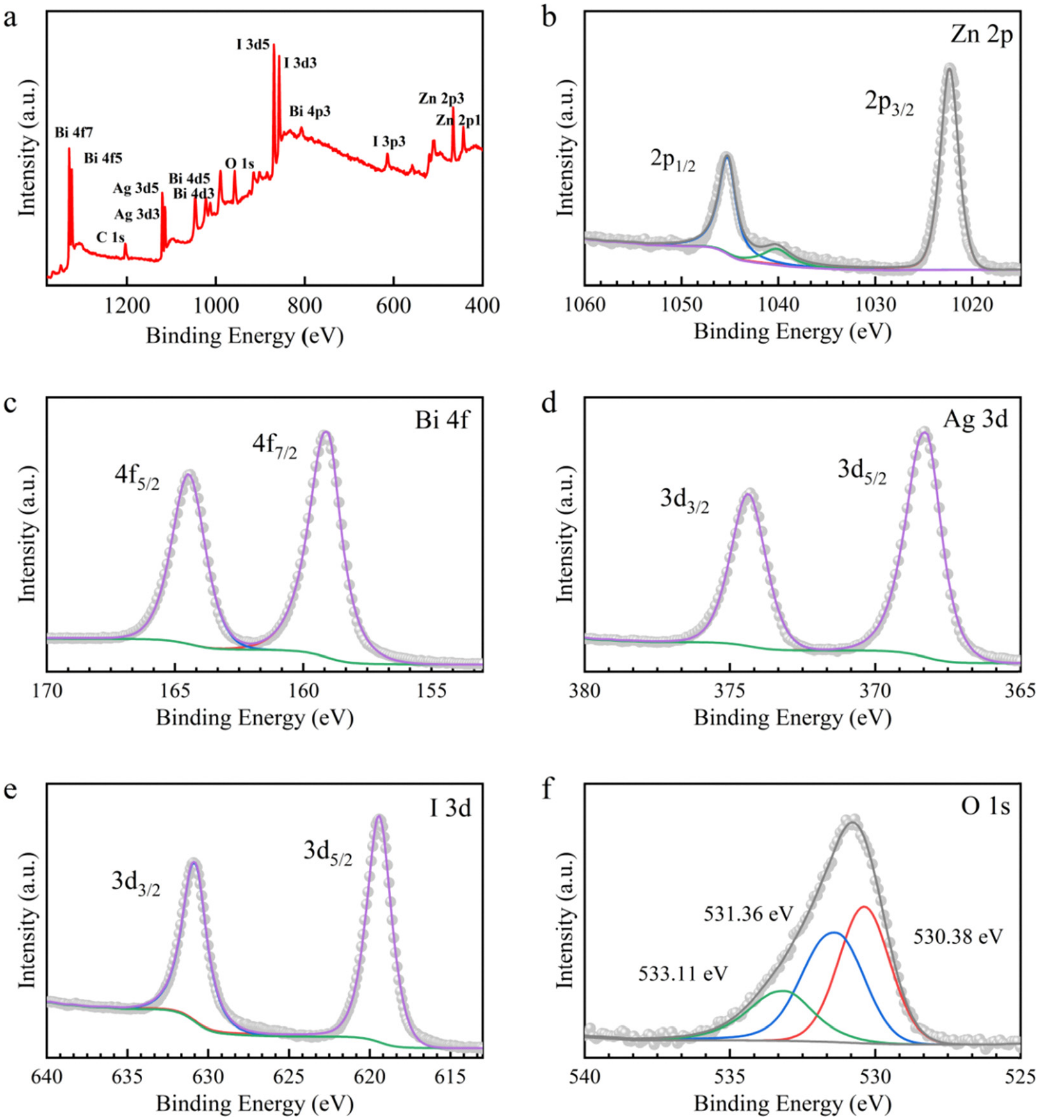

Fig. 4 XPS image of ZnO/BiOI/AgI. (a) Survey spectrum, (b) Zn 2p, (c) Bi 4f, (d) Ag 3d, (e) I 3d and (f) O 1s.

373.2 eV), suggesting that no elemental silver is present, which is consistent with the XRD results.[58] The I 3d spectrum (Fig. 4e) shows the peaks at 619.4 and 630.8 eV, attributed to I $3d_{5/2}$ and I $3d_{3/2}$ from iodine ions in BiOI and AgI.[59,60] The O 1s spectrum (Fig. 4f) features a typical peak that can be fitted as a Gaussian triplet. The peaks at 530.4, 531.4 and 533.1 eV are attributed to O^{2-} ions in BiOI, ZnO and O–H bonds from adsorbed water molecules.[61–63] The XPS results further corroborate the coexistence of ZnO, BiOI and AgI in the ZnO/BiOI/AgI heterojunction composite, consistent with the electron microscopy image and XRD pattern.

Moreover, EDS was employed to analyze the elemental composition and distribution within the ZnO/BiOI/AgI nanocomposites. A typical EDS sample, using a concentration of 30 mg L^{-1} for both ZnO and BiOI, was tested. Fig. 5 shows that in the ZnO/BiOI/AgI-3030 sample, the Zn element constitutes 38.92 wt%, Bi 10.11 wt%, Ag 15.91 wt%, O 16.39 wt%, and I 18.67 wt%. The EDS elemental mapping, presented in Fig. 5c–g, utilized distinct colors to represent the dispersion of different elements. It is evident that the Zn, Bi, Ag, O and I elements are uniformly dispersed throughout the nanocomposite material. These observations confirm the successful production of the nanocomposite catalysts.

3.1.4. BET analysis. The nitrogen adsorption–desorption isotherms of the as-prepared photocatalysts are presented in Fig. 6, with the inset illustrating the pore size distribution. The specific surface area, pore volume, and average pore size of all three nanocomposites are summarized in Table 1. According to the IUPAC classification, the isotherms of the ZnO, ZnO/BiOI and ZnO/BiOI/AgI samples all display type IV isotherms with a H3 hysteresis loop.[64–66] This indicates a mesoporous structure formed by the aggregation of plate-like materials, consistent with the SEM observations. The mesopores likely result from the self-assembly of ZnO nanosheets and the deposition of BiOI.[67–69] Table 1 shows the specific surface area, pore volume and average pore diameter of the three nanocomposites. There

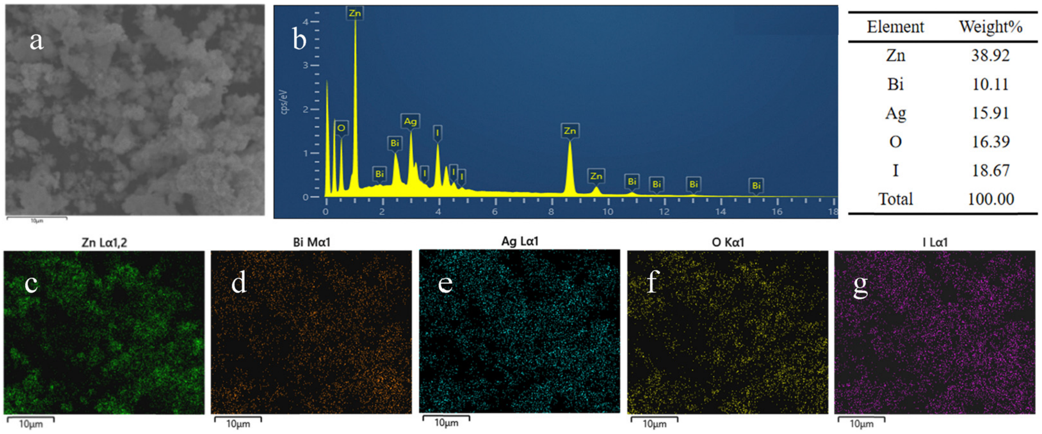

Element	Weight%
Zn	38.92
Bi	10.11
Ag	15.91
O	16.39
I	18.67
Total	100.00

Fig. 5 (a) and (b) EDS spectrum of ZnO/BiOI/AgI. (c)–(g) EDS elemental mapping of Zn, Bi, Ag, O and I in ZnO/BiOI/AgI.

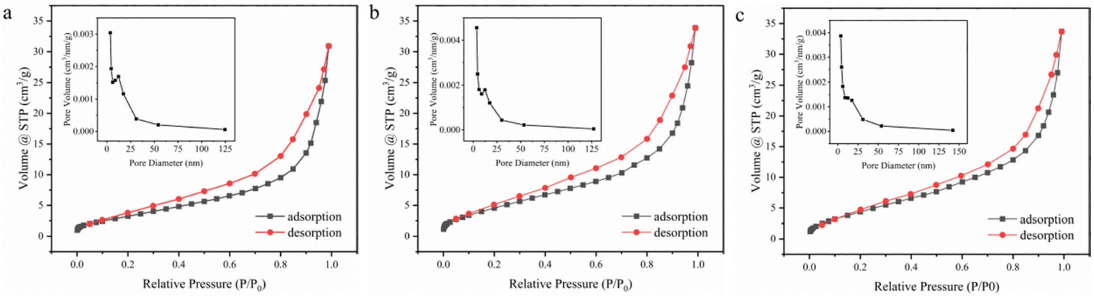

Fig. 6 Nitrogen adsorption–desorption isotherms and pore size distribution: (a) ZnO, (b) ZnO/BiOI and (c) ZnO/BiOI/AgI.

Table 1 Specific surface area, pore volume, and average pore size of nanocomposites

Sample	Specific surface area (m^2 g^{-1})	Pore volume (cm^3 g^{-1})	Average pore size (nm)
ZnO	13.098	0.046	3.636
ZnO/BiOI	18.775	0.049	3.637
ZnO/BiOI/AgI	18.483	0.049	3.621

is no significant change in the pore volume and average pore size after modifying ZnO, indicating that the introduction of BiOI and AgI does not markedly alter the pores. Moreover, the specific surface area of ZnO is 13.098 m^2 g^{-1}, that of ZnO/BiOI is 18.775 m^2 g^{-1}, and that of ZnO/BiOI/AgI is 18.483 m^2 g^{-1}. The addition of BiOI significantly increases the specific surface area, while AgI may cover part of the surface, slightly reducing it in the ternary materials.[70] A larger specific surface area can provide more active sites for photocatalysis, but it does not directly correlate with photocatalytic efficiency.[71] The high photocatalytic performance of the ZnO/BiOI/AgI ternary composite is likely due to the combination of the increased specific surface area and the reduced electron hole recombination rate.

3.1.5. UV-vis absorption spectra. The photoresponse range is a crucial factor for determining photocatalytic performance.[72] In Fig. 7a, the UV-vis diffuse reflectance spectra illustrate the optical absorption properties of ZnO, ZnO/BiOI, ZnO/AgI and ZnO/BiOI/AgI nanocomposites with various ratios. Pure ZnO exhibits strong absorption primarily in the ultraviolet region, with an absorption edge below 400 nm. This limits its photocatalytic activity to UV light. However, when BiOI is introduced, the absorption edge shifts significantly to 550 nm, indicating enhanced absorption in the visible light region. Similarly, the incorporation of AgI results in increased absorption around 450 nm. The ZnO/BiOI/AgI composite demonstrates the broadest absorption range, spanning both UV and visible regions. The extensive range is attributed to the formation of a heterojunction structure, which facilitates improved separation of e^-/h^+ pairs, thereby enhancing their photocatalytic activity under visible light.

Based on the UV-vis DRS spectra, the band gaps (E_g) of ZnO, BiOI and AgI were determined using Tauc's plots (Fig. 7b–d). The method involves the Kubelka–Munk formula (eqn (1)):

$$\alpha h\nu = A(h\nu - E_g)^{2/n} \tag{1}$$

where α is the optical absorption coefficient, h is the Planck constant, ν is the light frequency, A is a proportionality constant, E_g is the band gap energy, and n is equal to 1 or 4 for a direct or an indirect transition semiconductor, respectively. The n values are 1 for ZnO,[73] 4 for BiOI,[74] and 1 for AgI.[75] The E_g values of photocatalysts can be estimated by extrapolating the linear portion of the Tauc plots to intersect the horizontal axis. Thus, the E_g values of ZnO, BiOI and AgI were found to be 3.25, 1.86 and 2.78 eV, respectively, consistent with the previous reports.[76–78]

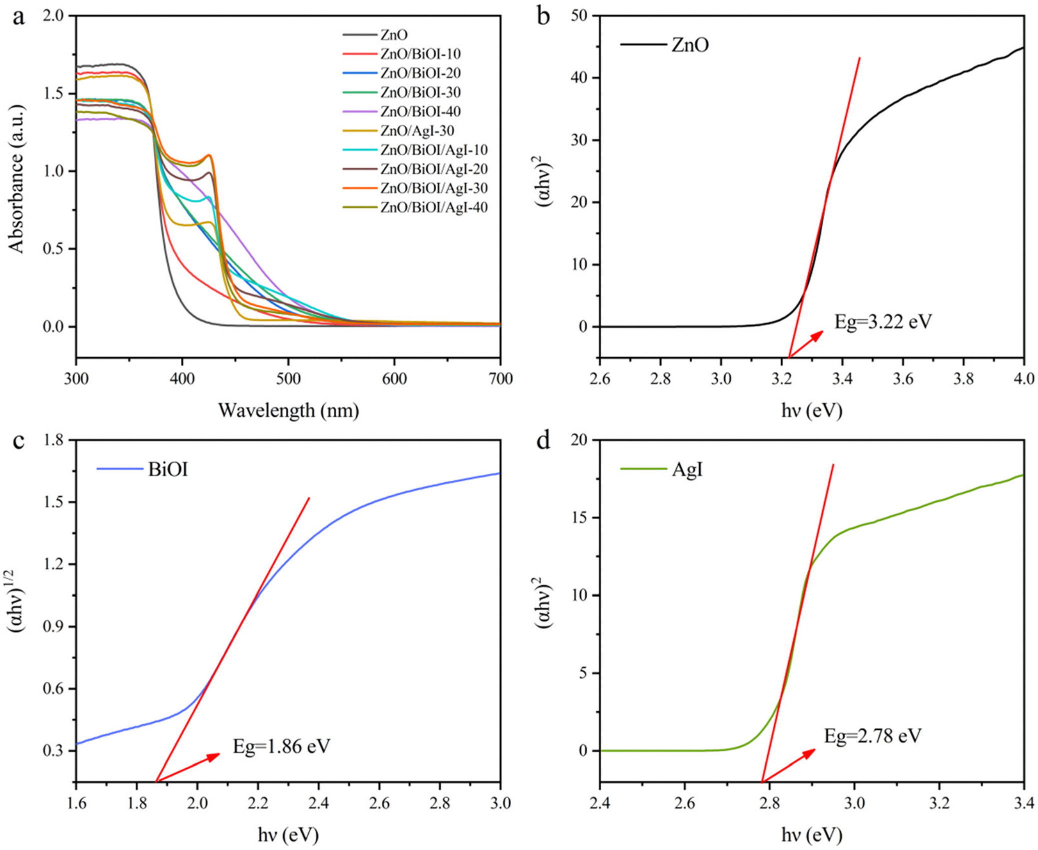

Fig. 7 UV-Vis DRS spectra and Tauc spectra of photocatalysts. (a) The UV-vis DRS spectra of ZnO, ZnO/BiOI, ZnO/AgI, and ZnO/BiOI/AgI nanocomposites with various compositions. Tauc spectra of (b) ZnO, (c) BiOI and (d) AgI.

3.2. Photocatalytic performance

The photocatalytic performance of the ZnO/BiOI/AgI composites was evaluated through the degradation of RhB organic dyes and antibiotics under visible light irradiation. RhB was selected as a model of organic pollutants for degradation. The UV-visible absorption spectrum of RhB exhibits a maximum absorption wavelength at 554 nm ($\lambda_{\max}$), which was used to monitor the concentration changes of RhB throughout the degradation process. Prior to light exposure, the photocatalysts were dispersed in the RhB solution and stirred for 60 minutes in the dark to achieve adsorption–desorption equilibrium. It is well known that pure RhB solution is inherently stable in nature.[79] As shown, the blank curve represents the RhB solution subjected to visible light irradiation in the absence of any catalyst, therefore, the influence of environmental factors such as visible light on its degradation is negligible. However, upon introducing different proportions of photocatalysts, a significant decrease in the RhB concentration over time is observed, as shown in Fig. 8a. This indicates that the photocatalysts play a crucial role in the degradation process. Due to its wide band gap, pure ZnO exhibits limited photocatalytic activity and is only capable of degrading a small fraction of the RhB dye. Specifically, pure ZnO degraded only 21.0% of the RhB solution after 180 minutes of visible light irradiation. The introduction of the BiOI composite into ZnO significantly enhanced the photocatalytic activity of the composite, as BiOI forms a heterojunction with ZnO, which promotes charge separation and reduces the recombination of photogenerated e^-/h^+ pairs. Among the ZnO/BiOI composite samples tested, the ZnO/BiOI-30 sample exhibited the highest degradation efficiency, degrading 54.3% of RhB under the same experimental conditions. To further improve the photocatalytic efficiency, AgI was introduced into the ZnO/BiOI-30 system, forming a ternary ZnO/BiOI/AgI composite. The addition of AgI further enhanced the photocatalytic activity, as AgI can also form a heterojunction with both ZnO and BiOI, further extending the absorption range into the visible light region and promoting more efficient charge separation. The degradation rates for RhB of ZnO/BiOI/AgI ternary composites were significantly higher compared to those of both the monomeric ZnO and binary ZnO/BiOI and ZnO/AgI composites, as shown in Fig. 8b. The optimal ZnO/BiOI/AgI sample exhibited a degradation rate of 98.1%, nearly completely degrading the RhB dye.

The kinetics of photocatalytic degradation were further examined using a first-order kinetic model, with the rate curves illustrated in Fig. 8c. The degradation followed first-order reaction kinetics, which can be described by eqn (2):

$$\ln(c_0/c) = k_{\mathrm{obs}}t \tag{2}$$

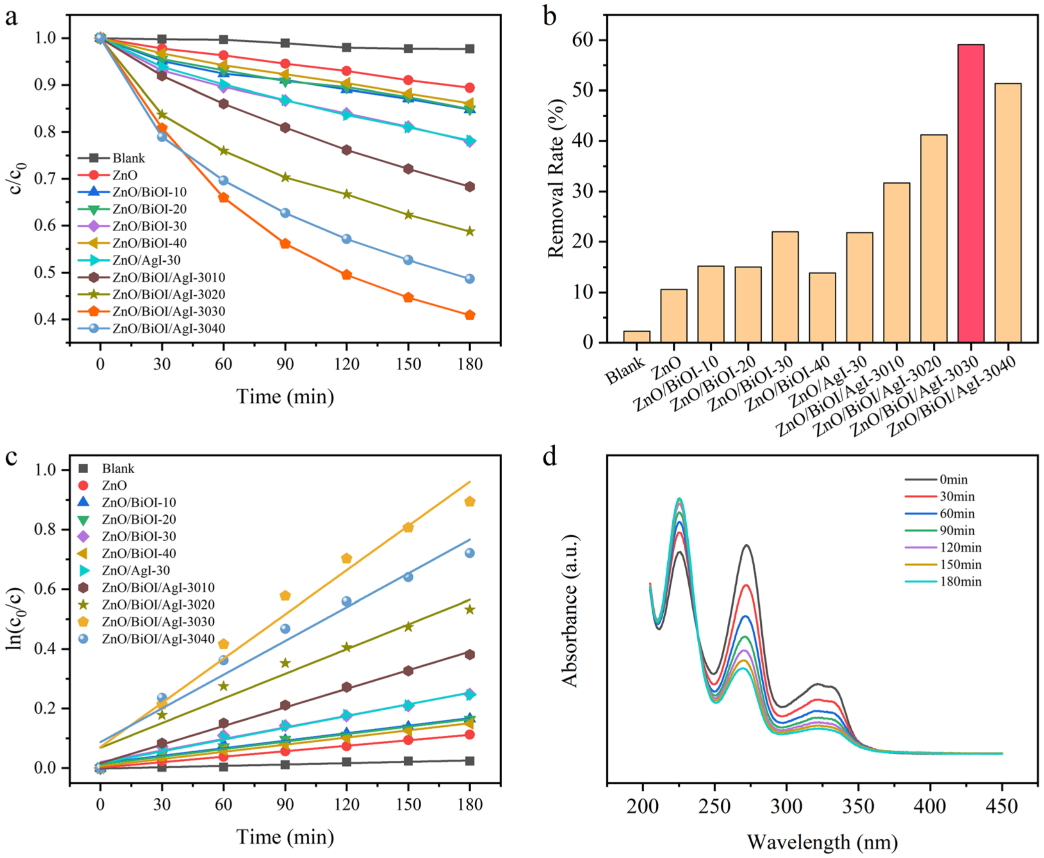

Fig. 8 Photocatalytic activity of different materials for degradation of RhB dyes under visible light. (a) Degradation curve of RhB dyes under visible light. (b) Degradation rate of RhB with different ratios of materials. (c) First-order kinetics for degradation of RhB dyes. (d) Time-resolved UV-vis absorbance spectra for the photocatalytic degradation of the RhB dye by the ZnO/BiOI/AgI-3030 sample at a 30-minute interval.

where c is the concentration of RhB solution during the reaction (mg L^{-1}), c_0 is the initial concentration (mg L^{-1}), k_{obs} is the reaction rate constant (min^{-1}), and t is the reaction time (min), respectively. For pure ZnO, a low rate constant of 0.0012 min^{-1} was obtained, indicating very weak photocatalytic activity. However, the incorporation of BiOI or AgI into the ZnO matrix significantly increased the reaction rate. The k_{obs} for the optimal ZnO/BiOI/AgI-3030 sample was measured to be 0.022 min^{-1}, which was 18.33 times higher than that of pure ZnO, demonstrating the superior photocatalytic efficiency of the ternary composite.

To further explore the dye degradation process, time-resolved UV-vis absorbance spectra of the RhB solution were recorded at 30-minute intervals during the photocatalytic degradation by the ZnO/BiOI/AgI-3030 sample (Fig. 8d). The gradual decrease in the absorption peak at 554 nm with increasing visible light irradiation time indicates the progressive breakdown of RhB molecules. After 180 minutes of visible light exposure, the absorption intensity had decreased to nearly zero. signifying almost complete degradation of RhB. Additionally, the color of the RhB solution, which was initially a deep pink, progressively faded and becomes nearly colorless after the complete degradation, as evidenced by the inset photographs in Fig. 8d. The results demonstrate that ZnO/BiOI/AgI nanocomposites effectively disrupt the molecular structure of RhB, leading to the complete degradation of contaminants.

In addition to RhB, the photocatalytic activity of the ZnO/BiOI/AgI composites was also evaluated for the degradation of NOR, a widely used antibiotic, under visible light irradiation. NOR was chosen due to its extensive application and environmental persistence, making it a significant pollutant of concern.[80] The UV-visible absorption spectrum of NOR shows a maximum absorption wavelength at 273 nm, which was employed to monitor the concentration changes of NOR throughout the degradation process. The degradation performance of the synthesized photocatalysts is illustrated in Fig. 9. The blank experiment confirmed that visible light and other environmental factors had a negligible effect on the degradation of NOR, indicating that photocatalysis is the key driver of degradation. As shown in Fig. 9a, pure ZnO exhibited limited photocatalytic activity, degrading only 10.6% of NOR solution after 180 minutes of visible light irradiation. This low efficiency can be attributed to the wide band gap of ZnO, which limits its ability to absorb visible light and generate sufficient electron–hole pairs. However, the introduction of BiOI into ZnO to form a heterojunction significantly enhanced the photodegradation performance. The ZnO/BiOI-30 composite exhibited an improved degradation efficiency, degrading 22.0% of NOR under the same experimental conditions. This improvement can be explained by the fact that BiOI and ZnO formed a

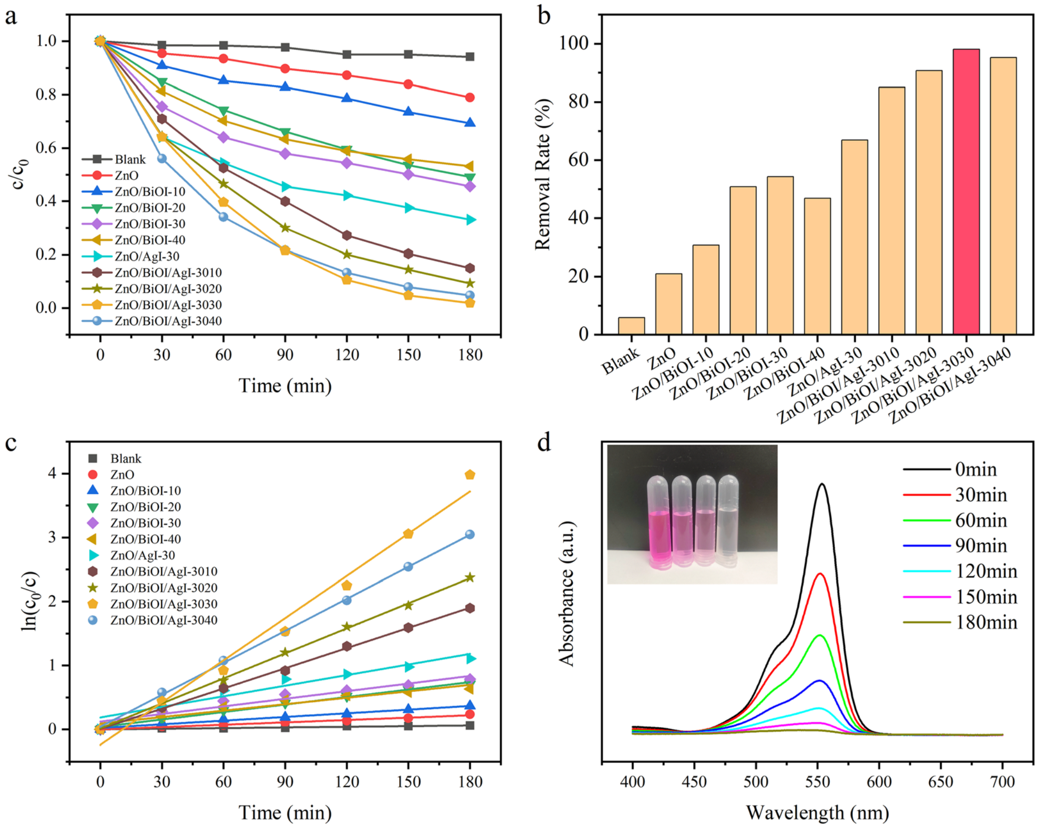

Fig. 9 Photocatalytic activity of different materials for NOR antibiotics under visible light. (a) Degradation curve of NOR antibiotics. (b) Degradation rate of NOR with different ratios of materials. (c) First-order kinetics for the photocatalytic degradation of NOR. (d) Time-resolved UV-vis absorbance spectra for the photocatalytic degradation of NOR antibiotics by the ZnO/BiOI/AgI-3030 sample at 30-minute intervals.

heterojunction structure to accelerate electron transfer and expand the photoresponse range, thereby enhancing the photocatalytic activity.

To further enhance the photocatalytic efficiency, AgI was introduced into the ZnO/BiOI-30 system, forming a ternary ZnO/BiOI/AgI composite. The addition of AgI further improved the degradation efficiency, with the photocatalytic performance increasing significantly across all ZnO/BiOI/AgI samples. As shown in Fig. 9b, the degradation rate of NOR increased with the AgI content, reaching an optimal value for the ZnO/BiOI/AgI-3030 sample. This sample achieved a 59.1% removal of NOR after 180 minutes under visible light irradiation. This superior performance of this ternary composite can be attributed to the optimized band gap and the enhanced charge separation efficiency facilitated by the ternary heterojunctions between ZnO, BiOI and AgI. However, a further increase in the AgI content beyond the optimal level resulted in a decline in performance, likely due to excessive AgI coverage hindering light absorption or increasing charge recombination.

The kinetics of NOR degradation were further analyzed using a first-order kinetic model, as described by eqn (2). The rate constant for ZnO was found to be 0.0006 min^{-1}, confirming its weak photocatalytic activity. In contrast, the ZnO/BiOI/AgI-3030 composite exhibited a much higher rate constant of 0.0049 min^{-1}, which is 8.17 times that of pure ZnO (Fig. 9c). This demonstrates the significant enhancement in photocatalytic efficiency achieved by the ternary composite.

To further explore the antibiotic degradation process, time-resolved UV-vis absorbance spectra of the NOR solutions were recorded at a 30 minute interval during the photocatalytic degradation by the ZnO/BiOI/AgI-3030 sample. According to Fig. 9d, the absorption peak at 273 nm gradually decreasing with increasing irradiation time indicates the progressive breakdown of NOR molecules. Although complete degradation of NOR was not achieved within the experimental timeframe, the results clearly show that the ZnO/BiOI/AgI-3030 composite significantly outperforms both the monomeric ZnO and binary ZnO/BiOI photocatalysts.

Overall, the ZnO/BiOI/AgI ternary composite materials exhibit excellent photocatalytic activity for the degradation of both dyes and antibiotics under visible light irradiation. The optimized heterojunctions formed in the ternary system adjust the band gap, improve the photoresponse range, enhance charge separation and improve photocatalytic efficiency, making them promising materials for the removal of organic pollutants from wastewater.

The stability and reusability of photocatalysts are crucial factors in determining their viability for practical applications.

Stable and reusable photocatalysts not only maintain high degradation efficiency over multiple cycles but also reduce operational costs, making them more economically feasible. To assess the stability and reusability of the ZnO/BiOI/AgI-3030 composite, recycling experiments were conducted using both RhB and NOR as model pollutants. The recycling experiments followed the same degradation protocol as that used for the initial photocatalytic degradation test. After each degradation cycle, the catalyst was recovered by centrifugation, washed with deionized water and dried before being reused in the next cycle. As shown in Fig. 10, the ZnO/BiOI/AgI-3030 composite exhibited excellent stability and reusability. After four consecutive cycles, the degradation rate for RhB remained above 90%, while the degradation rate for NOR remained above 50%. These results indicate only a slight reduction in photocatalytic activity, with the degradation rate decreasing by less than 10% after four cycles. The minor reduction in efficiency may be caused by the inevitable loss of mass during the recovery process or the potential adsorption of degradation by products on the active site of the material. The consistent photocatalytic performance indicates that the material maintains its functional properties after recycling experiments. This stability in performance suggests that the ZnO/BiOI/AgI-3030 composite retains its structural integrity and active sites throughout the cycles. Combined with its high reusability, this composite material emerges as a strong candidate for long-term applications, particularly in wastewater treatment, where sustained performance over multiple cycles is crucial. In summary, the ZnO/BiOI/AgI-3030 composite not only exhibits superior photocatalytic activity for the degradation of both organic dyes and antibiotics but also demonstrates excellent stability and reusability. These results highlight the potential of ZnO/BiOI/AgI-3030 as a highly efficient and sustainable photocatalyst for the treatment of organic pollutants in water.

3.3. Antibacterial experiment

The antibacterial properties of the synthesized catalytic materials were evaluated using the well diffusion method and the coating plate method. *E. coli* was selected as a representative G^- bacterium model, *S. aureus* as a G^+ bacterium model, and *MRSA* as a model for drug-resistant bacteria. These three bacterial strains were chosen due to their differing cell wall structures, which provide insight into the materials' antibacterial spectrum. In Fig. 11a, the well diffusion method was employed to assess antibacterial activity by measuring the inhibition zones formed around the catalysts, indicating bacterial growth suppression. Notably, the blank samples with artificially generated holes showed no inhibitory effect on bacterial growth. Pure ZnO exhibited the weakest antibacterial activity, with an inhibition zone of approximately 7 mm. The inhibition zones of ZnO/BiOI composites were 9.1 mm, 8.4 mm and 8.9 mm for *E. coli*, *S. aureus* and *MRSA*, respectively. Similarly, ZnO/AgI composites showed inhibition zones of 9.3 mm, 8.8 mm and 9.1 mm for the same bacterial strains. Consistent with the photodegradation results of organic pollutants, the antibacterial activity of the binary catalysts significantly improved upon the introduction of BiOI or AgI, demonstrating enhanced antibacterial efficacy. For the ternary composite heterojunctions, the ZnO/BiOI/AgI composites exhibited the largest inhibition zones, measuring 10.6 mm, 9.9 mm and 10.2 mm for *E. coli*, *S. aureus* and *MRSA*, respectively. These results suggest that the ternary material possesses the strongest antimicrobial activity, possibly due to the synergistic interactions among the semiconductor components, forming heterojunction structures that enhance bacterial death. It is also notable that all the catalyst materials displayed stronger antibacterial effects against G^- bacteria compared to G^+ bacteria. This difference in antibacterial activity may be attributed to the structural differences in their cell walls, particularly the thicker peptidoglycan layer in G^+ bacteria, which provides an additional barrier to antibacterial agents.[81] Additionally, the antibacterial effects on drug-resistant *MRSA* were comparable to those on non-resistant strains, suggesting that the ZnO/BiOI/AgI composite photocatalyst holds promise as an effective antibacterial agent, even against drug-resistant pathogens.

Furthermore, the photocatalytic antibacterial performance of the synthesized catalysts under visible light was assessed

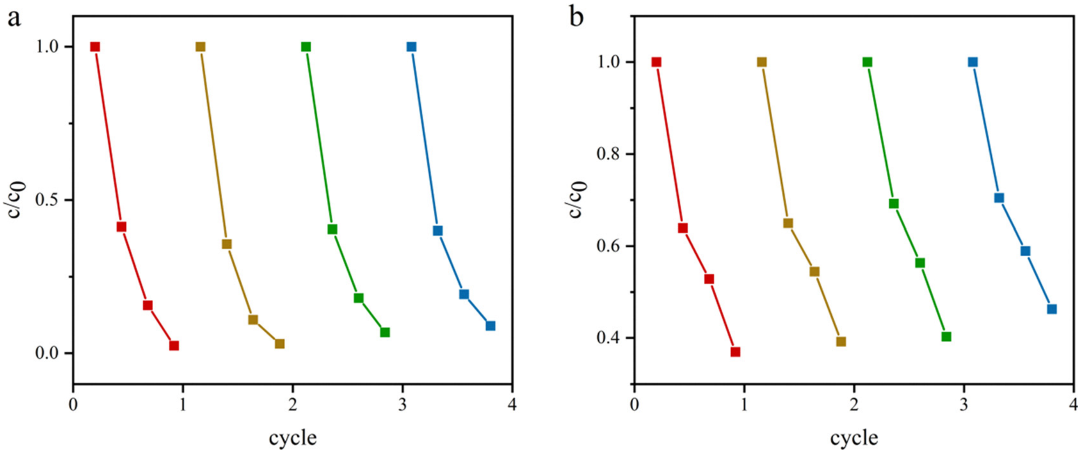

Fig. 10 Stability and reusability of the ZnO/BiOI/AgI-3030 photocatalyst after four cycles of use. (a) Photocatalytic degradation of RhB and (b) photocatalytic degradation of NOR.

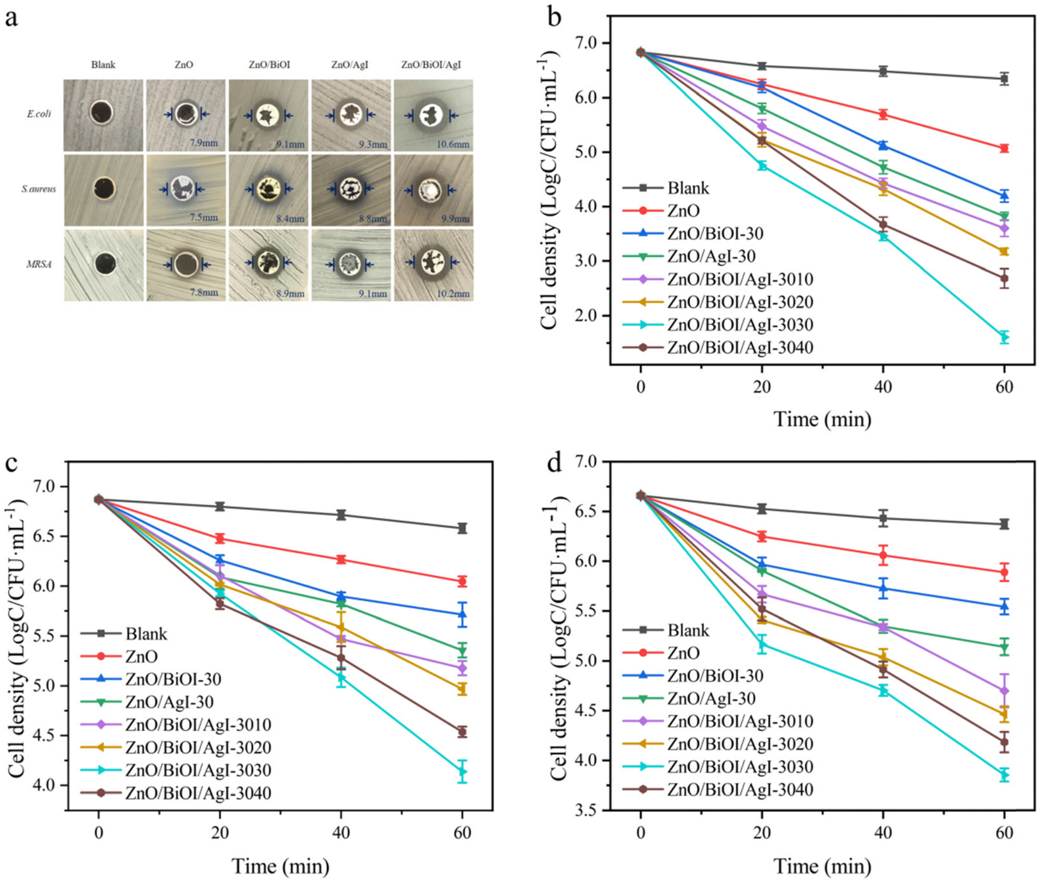

Fig. 11 Antibacterial properties of ZnO/BiOI/AgI composites against different bacteria. (a) Photographs of the synthesized catalysts' antibacterial inhibition zones against different strains. (b) The survival curves of *E. coli*, (c) *S. aureus*, and (d) *MRSA* with synthesized catalysts under visible light.

using the coating plate method against *E. coli*, *S. aureus* and *MRSA* bacteria, as shown in Fig. 11b–d. The growth of the bacterial solution after exposure to various photocatalysts is displayed in Fig. S1. The blank control showed minimal bacteria inactivated after 60 minutes of illumination, indicating that visible light alone did not significantly impact bacterial viability.[82] The combined catalysts demonstrated the most pronounced antibacterial effect against *E. coli*. Specifically, the bactericidal rate of the ZnO/BiOI/AgI-3030 composite reached 99.999% after 60 minutes of illumination, which was 3.15 times higher than that of ZnO and 2.61 times higher than that of ZnO/BiOI. For *S. aureus* and *MRSA* bacteria, the ZnO/BiOI/AgI-3030 composites also exhibited excellent antibacterial effects, with inhibition rates of 99.811% and 99.842%, respectively. Compared to *S. aureus*, the performance of the synthesized catalysts against *MRSA* was not diminished, indicating that the composite photocatalysts do not induce bacterial resistance. Additionally, the antibacterial effect of photocatalytic materials was generally stronger against G^- bacteria than G^+ bacteria, consistent with the inhibition zone results. This difference in antibacterial activity may be due to the thicker cell wall of G^+ bacteria, which offers greater resistance to the generated ROS.[83]

Among the three bacterial models, the bactericidal efficiency of the ternary composites surpassed that of both monadic and binary composites, with the ZnO/BiOI/AgI-3030 sample exhibiting the highest efficacy. This enhanced performance can be attributed to the introduction of narrow band gap materials into the wide band gap semiconductor materials, which facilitates the formation of a heterojunction structure, thereby narrowing the band gap width, enhancing the photocatalyst's light absorption, and promoting the rapid separation of e^-/h^+ pairs. This increases the generation of ROS, which can damage bacterial components such as the cell wall, membrane and proteins, ultimately leading to membrane disruption and cell death.[84] Moreover, silver-based semiconductor materials are widely recognized for their potent antibacterial properties.[85] The introduction of AgI further enhanced the bactericidal capabilities of the composite catalyst through a synergistic effect. Taken together, these results indicate that the ZnO/BiOI/AgI-3030 composite photocatalysts exhibit superior photocatalytic antibacterial properties compared to ZnO, ZnO/BiOI and ZnO/AgI, and thus hold great potential for application in pollutant degradation and disinfection.

3.4. Cytotoxicity assay

The cytotoxicity of the photocatalytic composite materials on DLD-1 cells was evaluated by using the CCK8 assay, a commonly used method for assessing cell viability *in vitro*.[86]

The cell survival rate was calculated using the following equation (eqn (3)):

$$\text{Cell survival }(\%) = \frac{\text{OD}_{\text{LL}} - \text{OD}_{\text{b.ctrl}}}{\text{OD}_{\text{n.ctrl}} - \text{OD}_{\text{b.ctrl}}} \quad (3)$$

where OD_{LL} is the absorbance value of cells treated with different concentrations of photocatalysts, $\text{OD}_{\text{b.ctrl}}$ is the absorbance value of blank control cells and $\text{OD}_{\text{n.ctrl}}$ is the absorbance value of cells treated with complete medium (CM) as the negative control. The results are shown in Fig. 12. Upon visible light irradiation, the cell survival rate of DLD-1 cells gradually decreased as the concentration of the composite photocatalyst increased. This indicates that all test photocatalysts exhibit cytotoxicity to DLD-1 cells in a concentration dependent manner. Among the tested heterojunction materials, ZnO/BiOI/AgI-3030 demonstrated the strongest cell anti-proliferation effect, with the highest toxicity at 250 μg mL^{-1}, where the survival rate of cancer cells was reduced to 11.21%. Comparatively, both binary and ternary composite heterojunction materials exhibited higher cytotoxicity against cancer cells than the pure ZnO. The cytotoxicity order of the tested photocatalysis was as follows: ZnO/BiOI/AgI-3030 > ZnO/BiOI/AgI-3040 > ZnO/BiOI/AgI-3020 > ZnO/BiOI/AgI-3010 > ZnOAgI-30 > ZnO/BiOI-30 > ZnO. This order aligns with the photocatalytic degradation results of organic pollutants and the photocatalytic antibacterial experiments. The observed cytotoxicity effects can be attributed to the generation of ROS under visible light irradiation, including $^{\bullet}\text{O}_2^{-}$, h^{+} and $^{\bullet}\text{OH}$, which are able to damage the cell membrane, induce DNA structural damage, and ultimately destroy the structure of cells.[87,88] The construction of the ternary complex heterojunction structure significantly enhanced the separation of e^{-} and h^{+}, resulting in increased ROS production and improved cytotoxic effects. This result suggests that the ternary ZnO/BiOI/AgI heterojunction materials have great potential for applications requiring photocatalytic cytotoxicity, such as cancer therapy or antimicrobial treatments.

3.5. Mechanism of the photocatalysts

3.5.1. Roles of reactive species. To further elucidate the mechanism of photodegradation on pollutants and the inactivation of bacteria, active species trapping experiments were conducted to identify the key reactive oxygen species (ROS) involved in the photocatalytic degradation process. It is established in photocatalysis that the main reactive species typically include holes (h^{+}), hydroxyl radicals ($^{\bullet}\text{OH}$) and superoxide anion radicals ($^{\bullet}\text{O}_2^{-}$).[89] The quenching experiments were performed by introducing specific scavengers into the RhB degradation system using the typical ZnO/BiOI/AgI-3030 composite as the photocatalyst. In these experiments, 0.1 mM of ammonium oxalate (AO) was employed to capture h^{+}, isopropanol (IPA) was used to scavenge $^{\bullet}\text{OH}$, and benzoquinone (BQ) was applied to trap $^{\bullet}\text{O}_2^{-}$.[90] As shown in Fig. 13a, the degradation curves of dyes in the presence of different scavengers demonstrate that the addition of each quencher significantly attenuated the photocatalytic performance, indicating the involvement of all three reactive species in the degradation process.

A more detailed analysis of the degradation rates (Fig. 13b) reveals that the introduction of IPA led to a minor reduction in the degradation rate, indicating that $^{\bullet}\text{OH}$ plays a partial role in the photodegradation. In contrast, the addition of AO caused a significant decrease in the degradation efficiency, suggesting

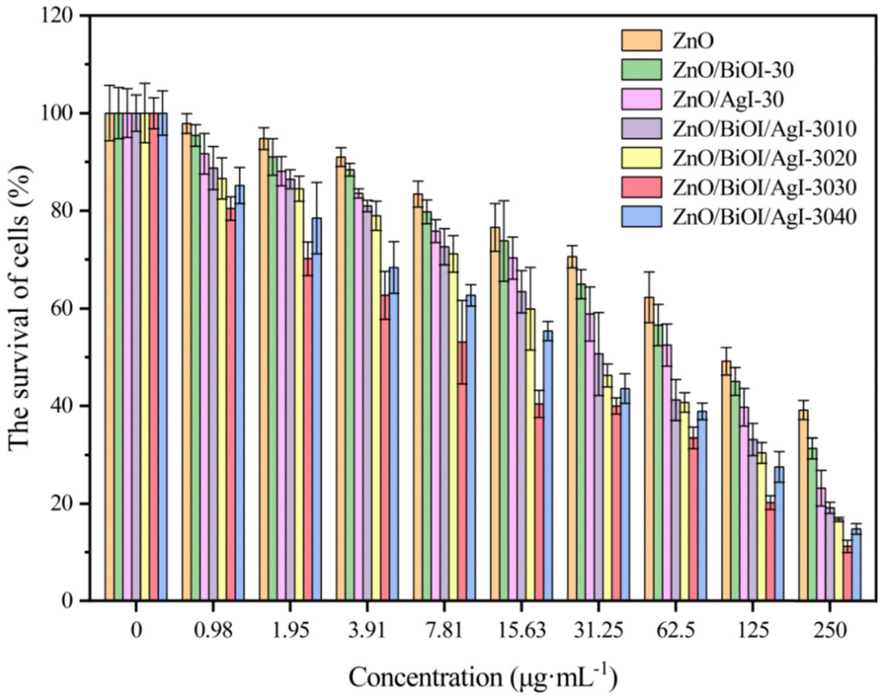

Fig. 12 Cytotoxicity of composite photocatalysts on DLD-1 cells.

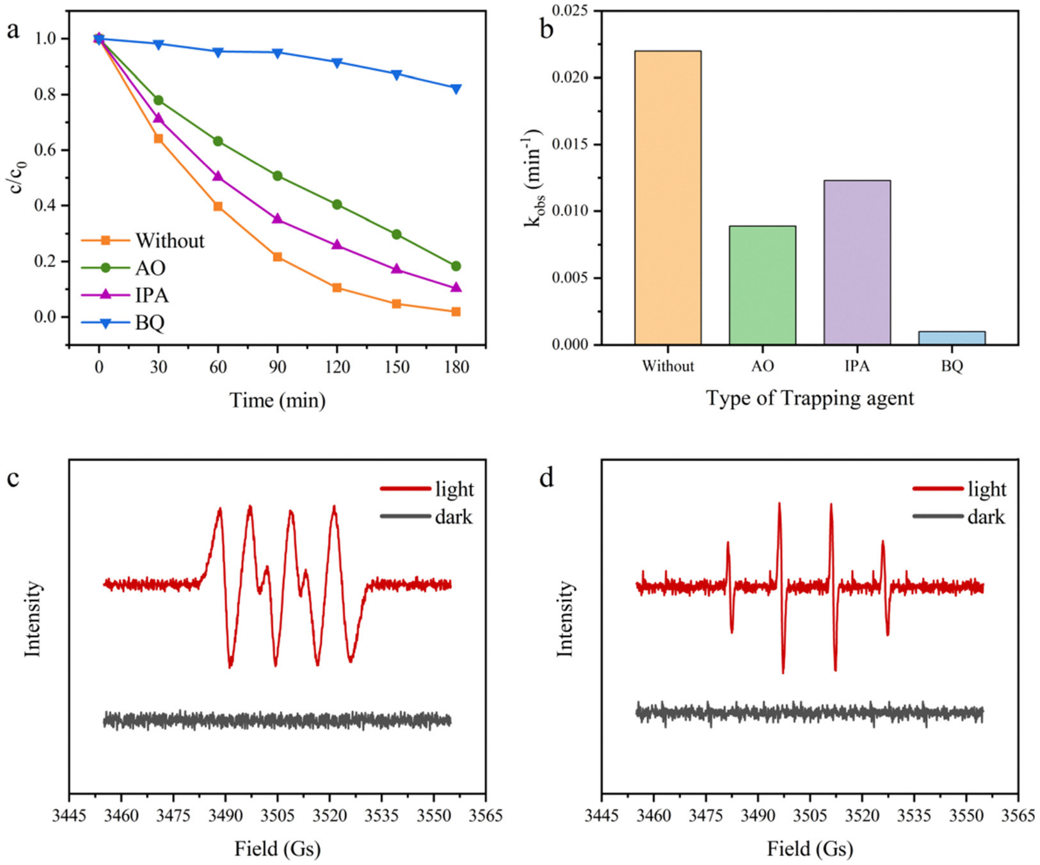

Fig. 13 The effect of reactive oxygen species on photocatalysis. (a) Degradation curves of RhB with different free radical trapping agents. (b) Degradation rate of RhB in free radical trapping experiments. (c) ESR spectrum of $^{\bullet}O_2^-$ labeled by DMPO. (d) ESR spectrum of $^{\bullet}$OH labeled by DMPO.

that h^+ is a major active species in the photocatalytic reaction. The most pronounced suppression of degradation was observed when BQ was added, indicating that $^{\bullet}O_2^-$ plays a primary role in the photocatalysis process. These results suggest that both h^+ and $^{\bullet}O_2^-$ are critical to the photocatalytic mechanism, with $^{\bullet}$OH playing a secondary role.

The ESR technique was employed using 5,5-dimethyl-1-dimethy-N-oxide (DMPO) as a spin-trapping agent to further confirm the generation of $^{\bullet}O_2^-$ and $^{\bullet}$OH radicals during photocatalysis. As illustrated in Fig. 13c and d, the ESR spectra of both DMPO-$^{\bullet}O_2^-$ and DMPO-$^{\bullet}$OH were recorded under visible light irradiation. No signals were detected in the absence of light, confirming that radical formation is light-dependent. After 10 minutes of visible light exposure, distinct signals were observed for $^{\bullet}O_2^-$ radicals, as detected by DMPO,[91] confirming the generation of $^{\bullet}O_2^-$ radicals in the system. Similarly, four characteristic peaks with an intensity ratio of 1 : 2 : 2 : 1 were detected for DMPO-$^{\bullet}$OH, indicating the formation of $^{\bullet}$OH radicals under visible light irradiation.[92] These findings are consistent with the results of the quenching experiments, further supporting the conclusion that h^+ and $^{\bullet}O_2^-$ are the dominate reactive species in the degradation and disinfection, with $^{\bullet}$OH contributing to a lesser extent. Thus, the concerted action of these ROS plays a vital role in both pollutant degradation and potential antibacterial activity.

3.5.2. Photoelectrochemical properties. The photoelectrochemical properties of the photocatalysts were analyzed to evaluate the effects of photogenerated carrier separation and transport efficiency of the heterojunction structures on photocatalytic performance under visible light irradiation. The TPR, EIS and PL characteristics of the ZnO, ZnO/BiOI, ZnO/AgI and ZnO/BiOI/AgI materials are presented in Fig. 14. The TPR spectra of ZnO/BiOI/AgI composites were measured to assess the transition efficiency of photogenerated e^-/h^+ pairs (Fig. 14a). During the TPR test, all samples were subjected to 20-second on–off cycles of Xe lamp irradiation. The corresponding photocurrent responses showed a rapid increase upon light exposure and immediate return to baseline in the absence of light, indicating the excellent stability of the photocurrent response.[93] A higher transient photocurrent response reflects a faster photocarrier transition rate, greater photocarrier generation, and improved photocatalytic potential.[94] Among the samples, pure ZnO exhibited the weakest photocurrent, indicating minimal photogenerated carrier production. The binary heterojunctions ZnO/BiOI and ZnO/AgI showed significantly improved photocurrent responses compared to pure ZnO, demonstrating enhanced transfer efficiency due to their heterojunction structures. Notably, the ZnO/BiOI/AgI ternary heterojunction displayed the highest photocurrent response, indicating superior photogenerated carrier production, an

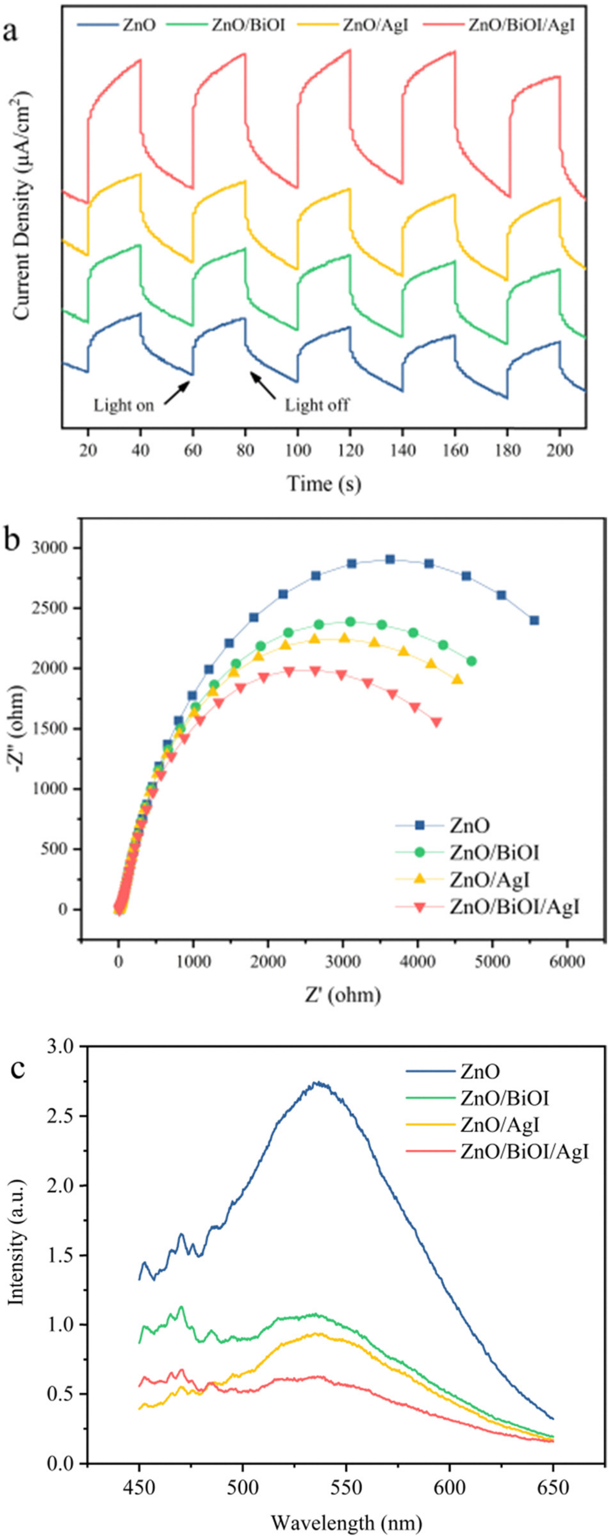

Fig. 14 Photoelectric performance of composite materials: (a) TPR spectra, (b) EIS Nyquist plot and (c) PL spectra.

increased transition rate, and greater photocatalytic potential under visible light.

The EIS Nyquist plot was used to evaluate the separation and transport of photogenerated carriers in different photocatalysts. The results, presented in Fig. 14b, reveal that a smaller arc diameter in the Nyquist plot corresponds to lower charge transfer resistance and more efficient separation of photoinduced carriers.[95] The arc diameters of the composite photocatalysts followed the trend: ZnO > ZnO/BiOI > ZnO/AgI > ZnO/BiOI/AgI. Notably, the ZnO/BiOI/AgI composite exhibited the smallest arc diameters, indicating the lowest charge transfer resistance and the highest efficiency of photogenerated carrier separation.

The PL spectra of ZnO/BiOI/AgI composites were recorded to further evaluate the separation efficiency of photogenerated e^-/h^+ pairs, a crucial factor influencing the photocatalytic performance. PL spectroscopy provides valuable insights into the recombination dynamics of the e^-/h^+ pairs, as the radiative recombination of these pairs leads to photon emission, resulting in photoluminescence.[96] In general, a reduction in PL intensity correlates with a lower recombination rate of photogenerated e^-/h^+ pairs, suggesting more efficient charge separation and, therefore, enhanced photocatalytic performance. As depicted in Fig. 14c, the PL spectra of pure ZnO, ZnO/BiOI, ZnO/AgI and ZnO/BiOI/AgI composites were recorded at room temperature under an excitation wavelength of 370 nm. Pure ZnO exhibits a pronounced photoluminescence peak at approximately 542 nm, which indicates a high recombination rate of the photogenerated charge carrier. In contrast, the PL intensity of the ZnO/BiOI and ZnO/AgI binary composites shows a significant reduction, suggesting that the binary heterojunction structure in these composites effectively promoted the separation of e^- and h^+, thereby reducing recombination. Notably, the ZnO/BiOI/AgI ternary composite exhibited the lowest PL intensity, signifying the most efficient charge separation among the examined samples.

These photoelectrochemical results are consistent with the findings from the photodegradation experiments. Enhanced charge separation correlates with a greater availability of free photogenerated e^- and h^+, which subsequently participate in the formation of ROS. ROS are known to play a pivotal role in degradation of organic pollutants and the inactivation of bacteria. Hence, the incorporation of BiOI and AgI into ZnO to form a ternary heterojunction structure significantly enhances charge carrier separation, which in turn improves both the photocatalytic and antibacterial performance of the ZnO/BiOI/AgI composite.

3.5.3. Possible photocatalytic mechanisms.

Based on the roles of photogenerated e^-/h^+ pairs and ROS in the photocatalytic process, a plausible mechanism for the ZnO/BiOI/AgI photocatalyst under visible light irradiation is proposed. The photocatalytic performance of the composite catalyst is strongly influenced by the relative energy band positions of each semiconductor material. The valence band (VB) and conduction band (CB) positions of the semiconductors were calculated using the Butler formula (eqn (4) and (5)):[97]

$$E_{\mathrm{VB}} = \chi - E_{\mathrm{e}} + 0.5E_{\mathrm{g}} \tag{4}$$

$$E_{\mathrm{CB}} = E_{\mathrm{VB}} - E_{\mathrm{g}} \tag{5}$$

Here E_{CB} and E_{VB} represent the CB and VB edge potentials, respectively, while χ denotes the absolute electronegativity of the semiconductors, and E_e refers to the energy of free electrons on the hydrogen scale (approximately 4.5 eV). The E_g values of ZnO, BiOI and AgI were calculated using the Kubelka–Munk formula (Fig. 7). For the ZnO semiconductor, E_g was calculated to be 3.25 eV, and χ was determined to be 5.79 eV.[98] Based on these values and eqn (3) and (4), the E_{VB} was calculated to be 2.92 eV and E_{CB} was calculated to be −0.34 eV. Similarly, for the BiOI semiconductor, E_g was determined to be 1.86 eV with χ of 5.99 eV,[99] resulting in E_{VB} of 2.42 eV and E_{CB} of 0.56 eV. For AgI, the E_g was found to be 2.78 eV and the χ was 5.48 eV,[100] with the corresponding E_{VB} and E_{CB} values calculated to be 2.37 eV and −0.41 eV, respectively.

Based on these energy levels, the possible e^- or h^+ transfer pathways are illustrated in Fig. 15. Before contact, ZnO, BiOI and AgI possess distinct band structures and Fermi levels. ZnO and AgI, as n-type semiconductors, have Fermi levels close to their CB, while BiOI, a p-type semiconductor, has its Fermi level close to its VB.[101,102] The Fermi level of BiOI is lower than those of ZnO and AgI. Upon contact, the difference in Fermi levels drives the diffusion of e^- from the n-type semiconductor (ZnO and AgI) to the p-type BiOI near the p–n interfaces, leading to the accumulation of the positive charge in the n-type semiconductors, enriching BiOI with e^- and ZnO/AgI with h^+.[103] This charge redistribution continues until Fermi level equilibrium is achieved with the Fermi level of BiOI shifting upwards and those of ZnO and AgI shifting downwards. The resulting charge separation establishes an internal electric field at the interfaces (ZnO–BiOI and BiOI–AgI contact),[104] which synergistically enhances the photocatalytic performance by promoting the migration of photogenerated carriers.

Under visible light, BiOI and AgI exhibit strong photoresponsiveness, while ZnO shows a negligible response. Under light irradiation, the e^- in the VB of BiOI and AgI are excited to their CB. Driven by the internal electric field, the e^- in the CB of BiOI migrates to the CB of ZnO and AgI, while h^+ in the VB of AgI migrates to the VB of BiOI. This p–n-p heterojunction structure effectively separates the photogenerated carriers and reduces the recombination of e^- and h^+.

The CB potentials of both ZnO and AgI are more negative than the redox potential of $O_2/^{\bullet}O_2^-$ (−0.33 eV *vs.* NHE),[105] allowing the e^- in the CB of ZnO and AgI to react with O_2 to generate $^{\bullet}O_2^-$. Additionally, the VB potentials of BiOI and AgI are not more positive than the redox potential of $H_2O/^{\bullet}OH$ (2.72 eV *vs.* NHE),[106] thus insufficient to oxidize H_2O to $^{\bullet}OH$. The h^+ in the VB of BiOI directly oxidize and decompose organic pollutants. The proposed mechanism aligns well with free radical trapping experiment results and the ESR results, which confirms the generation of ROS during the photocatalytic process. The overall photocatalytic reaction can be summarized as follows (eqn (6)–(12)):

$$\mathrm{ZnO/BiOI/AgI} + h\nu \rightarrow \mathrm{ZnO/BiOI/AgI}(e^- + h^+) \tag{6}$$

$$H_2O + h^+ \rightarrow {}^{\bullet}OH + H^+ \tag{7}$$

$$OH^- + h^+ \rightarrow {}^{\bullet}OH + H^+ \tag{8}$$

$$O_2 + e^- \rightarrow {}^{\bullet}O_2^- \tag{9}$$

$${}^{\bullet}O_2^- + 2H^+ + e^- \rightarrow H_2O_2 \tag{10}$$

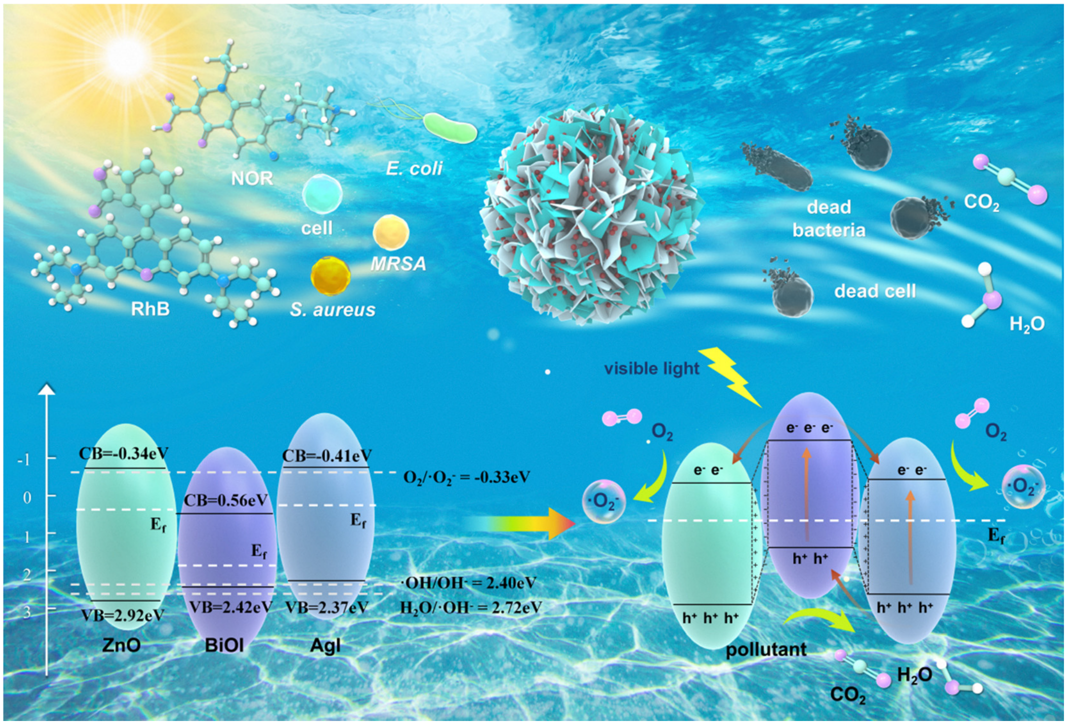

Fig. 15 A schematic diagram of photocatalytic mechanism of the ZnO/BiOI/AgI photocatalyst for pollutant degradation and bacterial cell inactivation under visible light irradiation.

$$H_2O_2 + e^- \rightarrow {}^{\bullet}OH + OH^- \quad (11)$$

$${}^{\bullet}O_2^-/h^+/{}^{\bullet}OH + \text{pollutants} \rightarrow \text{degradation products} \quad (12)$$

In conclusion, the ZnO/BiOI/AgI ternary composite photocatalysts exhibit an enhanced photocatalytic degradation mechanism through the formation of an n–p–n heterojunction. The synergistic effect between the internal electric field and the band alignment accelerates the movement of e^- and h^+ across the heterojunction,[107] facilitating the rapid separation of photogenerated carriers and consequently enhancing the overall photocatalytic performance.

3.5.4. RhB degradation pathway analysis. To elucidate the degradation mechanism of RhB by the ZnO/BiOI/AgI-3030 photocatalyst, the intermediates generated during the degradation process were analyzed using high performance liquid chromatography-mass spectrometry (LC–MS). Fig. S2 illustrates the mass spectra during RhB degradation and the detected degradation intermediates are listed in Table S3. Based on the mass spectra of pollutant solutions at various reaction times and previous studies,[108,109] a possible degradation pathway was proposed, as illustrated in Fig. 16. The degradation process of RhB (*m*/*z* = 443.19) proceeded through a series of sequential steps, including *N*-de-ethylation, chromophore cracking, ring opening and mineralization.[110] Initially, the degradation reaction was triggered by the oxidative attack of ROS generated by the ZnO/BiOI/AgI-3030 photocatalyst on the *N*-ethyl groups of RhB. This stepwise removal of the four *N*-ethyl groups produced intermediates with *m*/*z* values of 415.16, 387.13, 318.26 and 301.14, respectively. As the reaction progresses, these intermediates underwent further oxidation by ROS, resulting in the cleavage of the chromophore structure and the formation of smaller intermediates with *m*/*z* of 297.08, 274.24, 231.83, 223.04, 153.93, *etc.* With continued oxidation, the aromatic rings of these intermediates were opened, yielding low-molecular-weight alcohols and acids with *m*/*z* values of 149.93, 130.14, 102.11, and 74.05. Ultimately, these small molecule intermediates were further oxidized and mineralized into inorganic products, such as H_2O, CO_2, NH_4^+ and other harmless byproducts. This comprehensive pathway highlights the effective role of the ZBA-3030 photocatalyst in facilitating the stepwise decomposition and mineralization of RhB through ROS-mediated reactions. The results underscore the potential of ZnO/BiOI/AgI ternary heterojunctions as highly efficient photocatalysts for degradation of organic dyes, offering a promising strategy for wastewater treatment applications.

4. Conclusion

In this study, the n–p–n type heterojunction ZnO–BiOI–AgI composite photocatalysts were successfully synthesized *via* a facile precipitation method. The ternary composites exhibited a unique flower-like spherical structure composed of nanosheets and nanorods. The formation of the heterojunction structure significantly extended the visible light absorption range of the composite to 550 nm and reduced the recombination rate of photogenerated electron–hole pairs, demonstrating the superior photocatalytic properties of the n–p–n type heterojunctions.

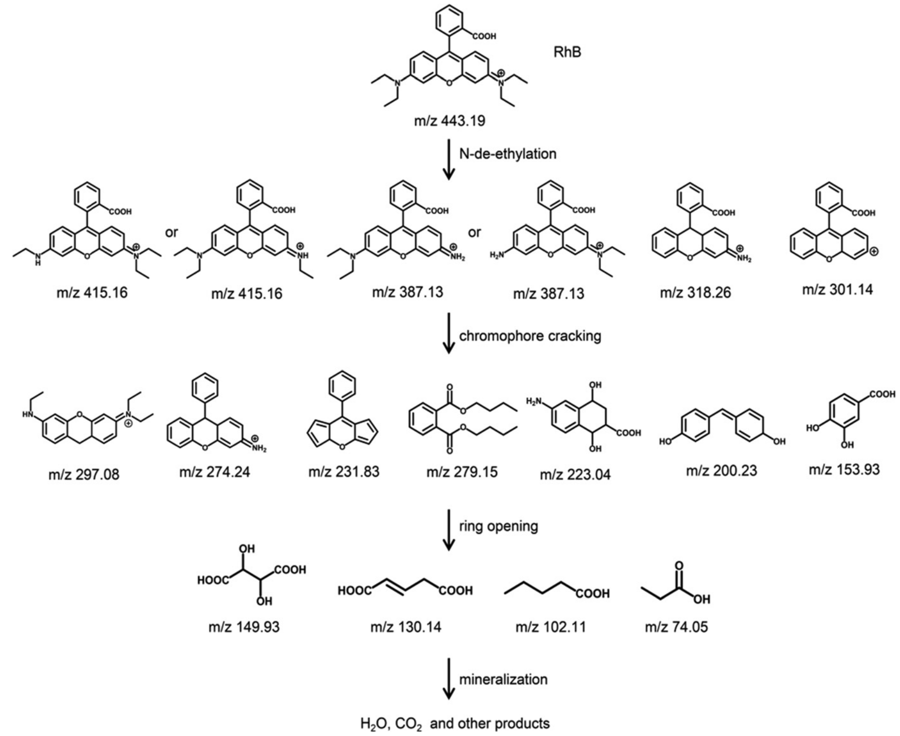

Fig. 16 The possible degradation pathway of RhR by the ZnO/BiOI/AgI-3030 photocatalyst.

Photocatalytic degradation experiments using RhB and NOR as model pollutants revealed that the ZnO/BiOI/AgI-3030 composite exhibited the best performance, achieving 98.1% degradation of RhB and 59.1% degradation of NOR under visible light irradiation. The composite also demonstrated excellent stability and reusability for multiple cycles. Furthermore, antibacterial experiments using *E. coli*, *S. aureus* and *MRSA* as bacterial models showed that ZnO/BiOI/AgI-3030 exhibited superior antimicrobial performance, inactivating 99.999%, 99.811% and 99.842% of bacteria, respectively, under visible-light irradiation. Additionally, cytotoxicity tests revealed that ZnO/BiOI/AgI exhibited dose-dependent activity against DLD-1 cells with an inhibition efficiency of 88.79% at a concentration of 250 μg mL^{-1}.

Mechanistic studies confirmed that the photodegradation activity of ZnO/BiOI/AgI was primarily driven by ROS, including $^{\bullet}O_2^-$, h^+ and $^{\bullet}OH$, as evidenced by trapping experiments and ESR analysis. The calculated band gaps and energy band positions further elucidated the role of the n–p–n composite heterojunction structure in enhancing charge generation and facilitating effective charge transfer, thereby improving the overall photocatalytic activity. The intermediates formed during RhB degradation were identified by LC–MS, and the corresponding degradation pathways were proposed, involving sequential *N*-de-ethylation, chromophore cleavage, ring opening, and mineralization into harmless inorganic products.

In conclusion, this study successfully developed recyclable ternary heterojunction photocatalysts with excellent photocatalytic activity and antimicrobial activities under visible light. The results provide a deeper understanding of the mechanism underlying the enhanced performance of n–p–n heterojunctions and offer valuable insights into wastewater pollution control.

Conflicts of interest

The authors declare that they have no known competing financial interests or personal relationships that could have appeared to influence the work reported in this paper.

Data availability

All data is available in the manuscript and SI. See DOI: **https://doi.org/10.1039/d5ma00354g**.

Acknowledgements

The authors gratefully acknowledge the financial support from the Natural Science Foundation of Chongqing, China [grant number: cstc2021jcyj-msxmX1078], Special Support for Post-doctoral Research of Chongqing, China (2020) and Natural Science Foundation of China (51701131). The authors are also grateful for the support from the Core Facility Center (CFC) at Capital Medical University, Beijing Area Major Laboratory of Peptide and Small Molecular Drugs, Engineering Research Center of Endogenous Prophylactic of Ministry of Education of China.

References

1 N. Jiang, R. Shang, S. G. J. Heijman and L. C. Rietveld, High-silica zeolites for adsorption of organic micro-pollutants in water treatment: a review, *Water Res.*, 2018, **144**, 145–161.

2 F. Deng, H. Shi, Y. Guo, X. Luo and J. Zhou, Engineering paths of sustainable and green photocatalytic degradation technology for pharmaceuticals and organic contaminants of emerging concern, *Curr. Opin. Green Sustainable Chem.*, 2021, **29**, 100465.

3 L. Chen, B. Yang, P. Zhou, T. Xu, C. He, Y. Xu, W. Zhao and C. Zhao, A polyethersulfone composite ultrafiltration membrane with the in-situ generation of CdS nanoparticles for the effective removal of organic pollutants and photocatalytic self-cleaning, *J. Membr. Sci.*, 2021, **638**, 119175.

4 S.-Y. Hu, Y.-N. Sun, Z.-W. Feng, F.-O. Wang and Y.-K. Lv, Design and construction strategies to improve covalent organic frameworks photocatalyst's performance for degradation of organic pollutants, *Chemosphere*, 2022, **286**, 131646.

5 C. Fan, Y. Liang, H. Dong, J. Yang, G. Tang, W. Zhang, D. Kong, J. Li and Y. Cao, Guanidinium ionic liquid-controlled synthesis of zeolitic imidazolate framework for improving its adsorption property, *Sci. Total Environ.*, 2018, **640–641**, 163–173.

6 J. Geng, L. Lin, F. Gu and J. Chang, Adsorption of Cr(VI) and dyes by plant leaves: effect of extraction by ethanol, relationship with element contents and adsorption mechanism, *Ind. Crops Prod.*, 2022, **177**, 114522.

7 X. Peng, W. Liu, W. Liu, P. Zhao, X. Yu and Y. Wang, Fabrication of eco-friendly adsorbent derived from serpentine tailings for the removal of organic dyes, *Colloids Surf., A*, 2022, **643**, 128761.

8 T. Liu, L. Wang, X. Liu, C. Sun, Y. Lv, R. Miao and X. Wang, Dynamic photocatalytic membrane coated with $ZnIn_2S_4$ for enhanced photocatalytic performance and antifouling property, *Chem. Eng. J.*, 2020, **379**, 122379.

9 J. Lv, F. Sun, Z. Li, Y. Qin, R. Sheng and L. Sun, Comparative Study of the Effects of Drugs Targeting Adrenergic Receptors on the Early Life Stages of Zebrafish, *Toxics*, 2024, **12**, 583.

10 Q. Ma, N. Zhao, Y. Wei, S. Wang, D. Liu and P. Yuan, Efficient adsorption and separation of norfloxacin from water by allophane aerogel microspheres, *Sep. Purif. Technol.*, 2023, **327**, 124808.

11 N. Fang, Q. He, L. Sheng, Y. Xi, L. Zhang, H. Liu and H. Cheng, Toward broader applications of iron ore waste in pollution control: adsorption of norfloxacin, *J. Hazard. Mater.*, 2021, **418**, 126273.

12 J. Tang, R. Wang, M. Liu, Z. Zhang, Y. Song, S. Xue, Z. Zhao and D. D. Dionysiou, Construction of novel Z-scheme

Ag/$FeTiO_3$/Ag/$BiFeO_3$ photocatalyst with enhanced visible-light-driven photocatalytic performance for degradation of norfloxacin, *Chem. Eng. J.*, 2018, **351**, 1056–1066.

13 F. Sordello, P. Calza, C. Minero, S. Malato and M. Minella, More than One Century of History for Photocatalysis, from Past, Present and Future Perspectives, *Catalysts*, 2022, **12**(12), 1572.

14 J. Singh and R. K. Soni, Efficient charge separation in Ag nanoparticles functionalized ZnO nanoflakes/CuO nanoflowers hybrids for improved photocatalytic and SERS activity, *Colloids Surf., A*, 2021, **626**, 127005.

15 G. Ren, H. Han, Y. Wang, S. Liu, J. Zhao, X. Meng and Z. Li, Recent Advances of Photocatalytic Application in Water Treatment: A Review, *Nanomaterials*, 2021, **11**(7), 1804.

16 Z. Q. Huang, S. M. Zhao, J. Q. Chen, Y. Zhao and W. Y. Sun, Pillar-layered metal-organic frameworks for sensing specific amino acid and photocatalyzing Rhodamine B degradation, *Molecules*, 2022, **27**(21), 7551.

17 Y. M. Hunge, A. A. Yadav, S.-W. Kang, S. Jun Lim and H. Kim, Visible light activated MoS_2/ZnO composites for photocatalytic degradation of ciprofloxacin antibiotic and hydrogen production, *J. Photochem. Photobiol., A*, 2023, **434**, 114250.

18 S. Amiri, M. Chahkandi and M. Zargazi, Ag_2O@UiO-66 new thin film as p–n heterojunction: permanent photoreduction of hexavalent Cr, *RSC Adv.*, 2024, **14**(6), 3867–3877.

19 R. Mangiri, K. Subramanyam, J. Lee, M. K. Lee, C. Lee, M. S. Khan, N. Roy, S. W. Joo and E. Chung, Self-assembled flower-like $ZnIn_2S_4$ coupled with g-C_3N_4@ZIF-67 heterojunction for improved photocatalytic hydrogen performance, *Surf. Interfaces*, 2024, **49**, 104401.

20 H. Liu, B. Wang, M. Chen, H. Zhang, J. Peng, L. Ding and W. Wang, Simple synthesis of BiOAc/BiOBr heterojunction composites for the efficient photocatalytic removal of organic pollutants, *Sep. Purif. Technol.*, 2021, **261**, 118286.

21 Y. Lu, F. Ren, Y. Gao, S. Zhang, Y. Zhao, X. Feng and L. Chen, S-scheme ZnO/CBO heterojunction photocatalytic activation of peroxymonosulfate for efficient degradation of organic pollutants, *Appl. Surf. Sci.*, 2025, 163462.

22 R. Gusain, K. Gupta, P. Joshi and O. P. Khatri, Adsorptive removal and photocatalytic degradation of organic pollutants using metal oxides and their composites: a comprehensive review, *Adv. Colloid Interface Sci.*, 2019, **272**, 102009.

23 K. M. Lee, C. W. Lai, K. S. Ngai and J. C. Juan, Recent developments of zinc oxide based photocatalyst in water treatment technology: a review, *Water Res.*, 2016, **88**, 428–448.

24 A. Raja, N. Son, M. Swaminathan and M. Kang, Effective visible light-driven ternary composite of ZnO nanorod decorated Bi_2MoO_6 in rGO for reduction of hexavalent chromium, *J. Environ. Chem. Eng.*, 2021, **9**(4), 105467.

25 T. Chankhanittha and S. Nanan, Visible-light-driven photocatalytic degradation of ofloxacin (OFL) antibiotic and Rhodamine B (RhB) dye by solvothermally grown ZnO/Bi_2MoO_6 heterojunction, *J. Colloid Interface Sci.*, 2021, **582**, 412–427.

26 P. Porrawatkul, R. Pimsen, A. Kuyyogsuy, P. Rattanaburi and P. Nuengmatcha, Morphology-dependent photocatalytic performance of ZnO nanostructures in organic dye and antibiotic degradation, *Int. J. Environ. Sci. Technol.*, 2024, **21**(11), 7397–7414.

27 R. Thirugnanam, A. Kannan, S. Ramasundaram, S. Kumaravel, M. Altaf, T. H. Oh, S. Jayababu, S. Narayanasamy, T. Ganesamoorthy and M. Inbasekaran, Radiant synergy: illuminating methyl orange dye removal with g-C_3N_4/ZnO heterojunction photocatalyst, *Diamond Relat. Mater.*, 2024, **147**, 111325.

28 D. Jovanović, S. Bognár, V. Despotović, N. Finčur, S. Jakšić, P. Putnik, C. Deák, G. Kozma, B. Kordić and D. Šojić Merkulov, Banana Peel Extract-Derived ZnO Nanopowder: Transforming Solar Water Purification for Safer Agri-Food Production, *Foods*, 2024, **13**(16), 2643.

29 A. Shi, D. Sun, X. Zhang, P. Sun, X. A. Li, B. Xiong and X. Niu, Sandwich-Polarized Heterojunction: Efficient Charge Separation and Redox Capability Protection for Photocatalytic Overall Water Splitting, *ACS Appl. Mater. Interfaces*, 2022, **14**(28), 32018–32025.

30 N. Tian, H. Huang, S. Wang, T. Zhang, X. Du and Y. Zhang, Facet-charge-induced coupling dependent interfacial photocharge separation: a case of BiOI/g-C_3N_4 p–n junction, *Appl. Catal., B*, 2020, **267**, 118697.

31 Q. Zhao, L. Hao, F. Li, T. Liu, Y. He, J. Yang, Y. Zhang and Y. Lu, Piezo/photocatalytic activity of flexible BiOCl-BiOI films immobilized on SUS304 wire mesh, *J. Water Process Eng.*, 2021, **42**, 102105.

32 Z. Yuan and Z. Jiang, Applications of BiOX in the Photocatalytic Reactions, *Molecules*, 2023, **28**(11), 4400.

33 J. Liu, S. Zou, B. Lou, C. Chen, L. Xiao and J. Fan, Interfacial Electronic Interaction Induced Engineering of ZnO-BiOI Heterostructures for Efficient Visible-Light Photocatalysis, *Inorg. Chem.*, 2019, **58**(13), 8525–8532.

34 Z. Wei, N. Zheng, X. Dong, X. Zhang, H. Ma, X. Zhang and M. Xue, Green and controllable synthesis of one-dimensional Bi_2O_3/BiOI heterojunction for highly efficient visible-light-driven photocatalytic reduction of Cr(VI), *Chemosphere*, 2020, **257**, 127210.

35 Z. Zhu, F. Guo, A. Li, W. Xu and X. Zhang, Simple synthesis of BiOI/ZnO/rGO for efficient photocatalytic degradation of antibiotic chloramphenicol under visible light, *J. Environ. Sci.*, 2023, **134**, 65–76.

36 X.-J. Wen, C.-G. Niu, L. Zhang and G.-M. Zeng, Fabrication of SnO_2 Nanopaticles/BiOI n–p Heterostructure for Wider Spectrum Visible-Light Photocatalytic Degradation of Antibiotic Oxytetracycline Hydrochloride, *ACS Sustainable Chem. Eng.*, 2017, **5**(6), 5134–5147.

37 D. Yuan, L. Huang, Y. Li, H. Wang, X. Xu, C. Wang and L. Yang, A novel AgI/BiOI/pg-C_3N_4 composite with enhanced photocatalytic activity for removing methylene orange, tetracycline and E. coli, *Dyes Pigm.*, 2020, **177**, 108253.

38 C. Wang, X. Li, X. Lv, X. Huang, Y. Zhao, T. Deng, J. Zhang, J. Wan, Y. Zhen and T. Wang, Insight into photocatalytic

chlortetracycline degradation by WO_3/AgI S-scheme heterojunction: DFT calculation, degradation pathway and electron transfer mechanism, *J. Cleaner Prod.*, 2024, **472**, 143521.

39 J. Liu, Y. Li, X. Liu, J. Fu, J. Li, Y. Liu, H. Wang and S. Li, Synthesis of a novel flower-like $Bi_4Ti_3O_{12}$/AgI Z-type heterojunction for efficient photocatalytic removal of tetracycline antibiotic and RhB, *J. Water Process Eng.*, 2024, **67**, 106262.

40 J. Shang, R. Zhao, X. Sun, X. Hu, L. Jin, C. Quan and Y. Zhang, Enhanced bacterial disinfection of multi-drug resistance bacteria by PCN@AgI heterojunction under visible light irradiation, *Chem. Eng. J.*, 2024, **499**, 155791.

41 G. U. Rehman, M. H. Dzarfan Othman, R. A. Wahab, A. F. Ismail, P. S. Goh, I. Khan and M. Irfan, Enhancing photocatalytic performance: studying the synthesis and characterization of AgI-tuned TiO_2/ZnO hybrid ternary nanocomposites, *J. Phys. Chem. Solids*, 2024, **192**, 112104.

42 X.-J. Wen, C.-H. Shen, Z.-H. Fei, D. Fang, Z.-T. Liu, J.-T. Dai and C.-G. Niu, Recent developments on AgI based heterojunction photocatalytic systems in photocatalytic application, *Chem. Eng. J.*, 2020, **383**, 123083.

43 X. Wu, Y. Zhang, H. Wu, J. Guo, K. Wu and L. Zhang, Facile synthesis of multi-shelled AgI/ZnO composite as Z-scheme photocatalyst for efficient ciprofloxacin degradation and H2 production, *J. Mater. Sci.: Mater. Electron.*, 2021, **32**, 26241–26257.

44 H. Huang, N. Huang, Z. Wang, G. Xia, M. Chen, L. He, Z. Tong and C. Ren, Room-temperature synthesis of carnation-like ZnO@AgI hierarchical nanostructures assembled by AgI nanoparticles-decorated ZnO nanosheets with enhanced visible light photocatalytic activity, *J. Colloid Interface Sci.*, 2017, **502**, 77–88.

45 J. Liu, C. Meng, X. Zhang, S. Wang, K. Duan, X. Li, Y. Hu and H. Cheng, Direct Z-scheme In_2O_3/AgI heterojunction with oxygen vacancies for efficient molecular oxygen activation and enhanced photocatalytic degradation of tetracycline, *Chem. Eng. J.*, 2023, **466**, 143319.

46 S. Ghattavi and A. Nezamzadeh-Ejhieh, A double-Z-scheme ZnO/AgI/WO_3 photocatalyst with high visible light activity: experimental design and mechanism pathway in the degradation of methylene blue, *J. Mol. Liq.*, 2021, **322**, 114563.

47 M. Jahurul Islam, D. Amaranatha Reddy, N. S. Han, J. Choi, J. K. Song and T. K. Kim, An oxygen-vacancy rich 3D novel hierarchical MoS_2/BiOI/AgI ternary nanocomposite: enhanced photocatalytic activity through photogenerated electron shuttling in a Z-scheme manner, *Phys. Chem. Chem. Phys.*, 2016, **18**(36), 24984–24993.

48 A. Ali, M. Shoeb, B. Li and M. A. Khan, Photocatalytic degradation of antibiotic drug and dye pollutants under visible-light irradiation by reduced graphene oxide decorated MoO_3/TiO_2 nanocomposite, *Mater. Sci. Semicond. Process.*, 2022, **150**, 106974.

49 L. Ma, J. Duan, B. Ji, Y. Liu, C. Li, C. Li, W. Zhao and Z. Yang, Ligand-metal charge transfer mechanism enhances TiO_2/Bi_2WO_6/rGO nanomaterials photocatalytic efficient degradation of norfloxacin under visible light, *J. Alloys Compd.*, 2021, **869**, 158679.

50 J. Yang, H. Su, Y. Wu, D. Li, D. Zhang, H. Sun and S. Yin, Facile synthesis of kermesinus BiOI with oxygen vacancy for efficient hydrogen generation, *Chem. Eng. J.*, 2021, **420**, 127607.

51 Z. Xin, S. Wang, Q. He, X. Han, Z. Fu, X. Xu and X. Zhao, Preparation of a novel photocatalytic catalyst PW_9@ZnO/Ag and the photocatalytic degradation of butyl xanthate under visible light, *Environ. Res.*, 2022, **214**, 113776.

52 H. Liu, J. Cai, M. Luo, C. Chen and P. Hu, Novel mesoporous bismuth oxyiodide single-crystal nanosheets with enhanced catalytic activity, *RSC Adv.*, 2020, **10**(10), 5913–5918.

53 C. Ding, K. Fu, M. Wu, S. Gong, J. Liu, J. Shi and H. Deng, Photocatalytic performance and mechanism of AgI/Ag/ZnO composites as catalysts for the visible-light-driven degradation of naproxen, *J. Photochem. Photobiol., A*, 2021, **414**, 113283.

54 B. P. Mabuea, R. E. Kroon, B. M. Sondezi and O. M. Ntwaeaborwa, Sol-gel synthesis and photoluminescent properties of metal oxide-metal oxide coupled nanocomposites, *Phys. B*, 2024, **675**, 415600.

55 M. Marny, M. Sowa, A. Kazek-Kęsik, K. Rokosz, S. Raaen, P. Chapon, R. Viter, R. Pshenychnyi, W. Simka and J. Michalska, Shaping the Structure and Properties of TiO_2–ZnO Oxide Coatings Produced by Plasma Electrolytic Oxidation on Titanium Substrate, *Materials*, 2023, **16**(23), 7400.

56 J. Ding, G. Su, Y. Zhou, H. Yin, S. Wang, J. Wang and W. Zhang, Construction of Bi/BiOI/BiOCl Z-scheme photocatalyst with enhanced tetracycline removal under visible light, *Environ. Poll.*, 2024, **341**, 122942.

57 P. Kamakshi, C. Joshitha, S. Chella and S. Selvaraj, Synthesis, characterization of BiOI/rGO nanocomposite and its photocatalytic functionality analysis under visible light, *Inorg. Chem. Commun.*, 2023, **150**, 110545.

58 X. Zhu, J. Wang, D. Yang, J. Liu, L. He, M. Tang, W. Feng and X. Wu, Fabrication, characterization and high photocatalytic activity of Ag–ZnO heterojunctions under UV-visible light, *RSC Adv.*, 2021, **11**(44), 27257–27266.

59 W. Wang, D. Ma, Y. Dai, Q. Wang, H. Xu, C. Yuan, X. Zhang, P. Dong and X. Xi, Fabrication of BiOI–C_3N_5 heterostructure with enhanced visible-light efficiency in photocatalytic antibiotics degradation, *Colloids Surf., A*, 2023, **675**, 131938.

60 X. Liu, Y. Zhong, H. Feng, Y. Zhao, Q. Li and T. Huang, Synthesis of novel AgI/BiOI nanocomposites and their high-efficiency visible-light-driven photocatalytic degradation performance for norfloxacin, *New J. Chem.*, 2024, **48**(2), 800–810.

61 Y. Long, L. Li, L. Zhou, S. Zhang, L. Wang, Z. Zheng, S. Wu, Y. Hei and F. Jiang, Fabrication of the AgI/BiOI/$BiPO_4$ multi-heterojunction with high photocatalytic activity, *Mater. Res. Bull.*, 2020, **126**, 110787.

62 X. Yu, H. Chen, Q. Ji, Y. Chen, Y. Wei, N. Zhao and B. Yao, p-Cu_2O/n-ZnO heterojunction thin films with enhanced photoelectrochemical properties and photocatalytic activities for norfloxacin, *Chemosphere*, 2021, **267**, 129285.

63 J. Tang, Y. Xue, C. Ma, S. Zhang and Q. Li, Facile preparation of BiOI/T-ZnOw p–n heterojunction photocatalysts with enhanced removal efficiency for rhodamine B and oxytetracycline, *New J. Chem.*, 2022, **46**(27), 13010–13020.

64 H. Adamu, P. Dubey and J. A. Anderson, Probing the role of thermally reduced graphene oxide in enhancing performance of TiO_2 in photocatalytic phenol removal from aqueous environments, *Chem. Eng. J.*, 2016, **284**, 380–388.

65 B. Zhai, Y. Chen and Y. Liang, In situ preparation of Ag_3VO_4/MOFs composites with enhanced visible-light-driven catalytic activity, *J. Nanopart. Res.*, 2019, **21**, 1–15.

66 F. Chen, X. Jin, Y. Cao, D. Jia, A. Liu, R. Wu and M. Long, Effects of the synthesis conditions on the photocatalytic activities of sulfide-graphene oxide composites, *Dyes Pigm.*, 2019, **162**, 177–188.

67 L. Huang, W. Fang, Y. Yang, J. Wu, H. Yu, X. Dong, T. Wang, Z. Liu and B. Zhao, Three-dimensional MoO_3 nanoflowers assembled with nanosheets for rhodamine B degradation under visible light, *Mater. Res. Bull.*, 2018, **108**, 38–45.

68 F. Chen, P. Fang, Y. Gao, Z. Liu, Y. Liu and Y. Dai, Effective removal of high-chroma crystal violet over TiO_2-based nanosheet by adsorption–photocatalytic degradation, *Chem. Eng. J.*, 2012, **204–206**, 107–113.

69 T.-W. Sun, Y.-J. Zhu, C. Qi, G.-J. Ding, F. Chen and J. Wu, α-Fe_2O_3 nanosheet-assembled hierarchical hollow mesoporous microspheres: microwave-assisted solvothermal synthesis and application in photocatalysis, *J. Colloid Interface Sci.*, 2016, **463**, 107–117.

70 F. Vosoughi, A. Habibi-Yangjeh, S. Asadzadeh-Khaneghah, S. Ghosh and T. Maiyalagan, Novel ternary g-C_3N_4 nanosheet/Ag_2MoO_4/AgI photocatalysts: impressive photocatalysts for removal of various contaminants, *J. Photochem. Photobiol., A*, 2020, **403**, 112871.

71 M. Azami, M. Haghighi and S. Allahyari, Sono-precipitation of Ag_2CrO_4-C composite enhanced by carbon-based materials (AC, GO, CNT and C_3N_4) and its activity in photocatalytic degradation of acid orange 7 in water, *Ultrason. Sonochem.*, 2018, **40**, 505–516.

72 X. Ning, Q. Peng, B. Zeng, X. Deng and L. Li, Ag_3PO_4/g-C_3N_4/$Zn_3(PO_4)_2$ catalyst with ternary heterostructure and Z-scheme/type II dual pathway mechanism for high photocatalytic performance, *J. Alloys Compd.*, 2024, **976**, 173070.

73 G. Mamba, J. Kiwi, C. Pulgarin, R. Sanjines, S. Giannakis and S. Rtimi, Evidence for the degradation of an emerging pollutant by a mechanism involving iso-energetic charge transfer under visible light, *Appl. Catal., B*, 2018, **233**, 175–183.

74 Y. Wang, A. Zhang, D. Zhang, P. Zhou, R. Wang, J. Xiang, X. Zhang and S. Su, Ag_2CO_3 anchored on BiOI/$CoFe_2O_4$ composites with p–n-p heterojunctions: highly enhanced activity for photocatalytic oxidation of Hg^0 under fluorescent light irradiation, *Colloids Surf., A*, 2019, **579**, 123654.

75 H. Zhang, C.-G. Niu, X.-J. Wen, Y. Wang and G.-M. Zeng, Enhanced visible light photocatalytic activity of $CdMoO_4$ microspheres modified with AgI nanoparticles, *Catal. Commun.*, 2016, **86**, 124–128.

76 J. Chen, F. Liu, T. Abdiryim, H. Yin and X. Liu, ZnO–$Ti_3C_2T_X$ composites supported on polyacrylic acid/chitosan hydrogels as high-efficiency and recyclable photocatalysts for norfloxacin degradation, *Int. J. Biol. Macromol.*, 2024, **258**, 128912.

77 Y. Bu, J. Xu, Y. Li, Q. Liu and X. Zhang, Enhanced photocatalytic activity of BiOI under visible light irradiation by the modification of MoS_2, *RSC Adv.*, 2017, **7**(67), 42398–42406.

78 M. Midhu Francis, A. Thakur, A. Balapure, J. Ray Dutta and R. Ganesan, Fabricating effective heterojunction in metal-organic framework-derived self-cleanable and dark/visible-light dual mode antimicrobial CuO/AgX (X = Cl, Br, or I) nanocomposites, *Chem. Eng. J.*, 2022, **446**, 137363.

79 P. Suebsom, A. Phuruangrat, S. Suwanboon, S. Thongtem and T. Thongtem, Photocatalytic Degradation of Rhodamine B by Highly Effective Heterostructure Pd/Bi_2MoO_6 Nanocomposites Synthesized by Photoreduction Deposition Method, *J. Inorg. Organomet. Polym. Mater.*, 2020, **31**(1), 162–171.

80 Y. Lin, C. Yang, S. Wu, X. Li, Y. Chen and W. L. Yang, Construction of Built-In Electric Field within Silver Phosphate Photocatalyst for Enhanced Removal of Recalcitrant Organic Pollutants, *Adv. Funct. Mater.*, 2020, **30**(38), 2002918.

81 A. R. Mendes, C. M. Granadeiro, A. Leite, E. Pereira, P. Teixeira and F. Poças, Optimizing Antimicrobial Efficacy: Investigating the Impact of Zinc Oxide Nanoparticle Shape and Size, *Nanomaterials*, 2024, **14**(7), 638.

82 X. Zhang, J. Zhang, J. Yu, Y. Zhang, F. Yu, L. Jia, Y. Tan, Y. Zhu and B. Hou, Enhancement in the photocatalytic antifouling efficiency over cherimoya-like $InVO_4$/$BiVO_4$ with a new vanadium source, *J. Colloid Interface Sci.*, 2019, **533**, 358–368.

83 S. Sathiyavimal, S. Vasantharaj, D. Bharathi, M. Saravanan, E. Manikandan, S. S. Kumar and A. Pugazhendhi, Biogenesis of copper oxide nanoparticles (CuONPs) using Sida acuta and their incorporation over cotton fabrics to prevent the pathogenicity of Gram negative and Gram positive bacteria, *J. Photochem. Photobiol., B*, 2018, **188**, 126–134.

84 B. Leng, X. Zhang, S. Chen, J. Li, Z. Sun, Z. Ma, W. Yang, B. Zhang, K. Yang and S. Guo, Highly efficient visible-light photocatalytic degradation and antibacterial activity by GaN:ZnO solid solution nanoparticles, *J. Mater. Sci. Technol.*, 2021, **94**, 67–76.

85 P. P. Li, H. X. Wu and A. Dong, Ag/AgX nanostructures serving as antibacterial agents: achievements and challenges, *Rare Met.*, 2022, 1–21.

86 J. Zhang, X. Liu, X. Wang, L. Mu, M. Yuan, B. Liu and H. Shi, Carbon dots-decorated $Na_2W_4O_{13}$ composite with WO_3 for highly efficient photocatalytic antibacterial activity, *J. Hazard. Mater.*, 2018, **359**, 1–8.

87 B. Sahoo, S. K. Rath, B. B. Champati, L. L. Panigrahi, A. K. Pradhan, S. Nayak, B. R. Kar, S. Jha and M. Arakha, Photocatalytic activity of biosynthesized silver nanoparticle

fosters oxidative stress at nanoparticle interface resulting in antimicrobial and cytotoxic activities, *Environ. Toxicol.*, 2023, **38**(7), 1577–1588.

88 S. Krishnan, S. Murugesan, V. Vasanthakumar, A. Priyadharsan, M. Alsawalha, T. Alomayri and B. Yuan, Facile green synthesis of $ZnFe_2O_4$/rGO nanohybrids and evaluation of its photocatalytic degradation of organic pollutant, photo antibacterial and cytotoxicity activities, *Colloids Surf., A*, 2021, **611**, 125835.

89 F. Mohamadpour and A. M. Amani, Photocatalytic systems: reactions, mechanism, and applications, *RSC Adv.*, 2024, **14**(29), 20609–20645.

90 H. Astaraki, S. M. Masoudpanah and S. Alamolhoda, Effects of ethylene glycol contents on phase formation, magnetic properties and photocatalytic activity of $CuFe_2O_4/Cu_2O/Cu$ nanocomposite powders synthesized by solvothermal method, *J. Mater. Res. Technol.*, 2021, **14**, 229–241.

91 Y. Huang, P. Zhao, H. Miao, S. Shao, L. Wang, Y. Chen, C. Jia and J. Xia, Organic–inorganic TCPP/BiOCl hybrids with accelerated interfacial charge separation for boosted photocatalytic performance, *Colloids Surf., A*, 2021, **616**, 126367.

92 L. Huang, J. Liu, Y. Li, L. Yang, C. Wang, J. Liu, H. Li and L. Huang, Enhancement of photocatalytic activity of Z-scheme BiO_{2-x}/BiOI heterojunction through vacancy engineering, *Appl. Surf. Sci.*, 2021, **555**, 149665.

93 R. Yang, G. Lu, H. Liang, Z. Li, J. Liang and Z. Chen, Enhancing the Photocatalytic Performance for Norfloxacin Degradation by Fabricating S-Scheme ZnO/BiOCl Heterojunction, *Molecules*, 2024, **29**(19), 4738.

94 H. R. Hua, K. Ye, H. Y. Chen, F. Y. Wang, Y. T. Hua, Q. F. Shi, H. Y. Yu, R. G. Lv and M. Chen, ZnO@ZnS core–shell nanorods with homologous heterogeneous interface to enhance photocatalytic hydrogen production, *Colloids Surf., A*, 2022, **652**, 129844.

95 M. Bashiri, M. Hosseini-Sarvari, Y. Gu and D. Zheng, Removal of hazardous diethyl phthalate released from plastics using mesoporous graphitic carbon nitride boosted with ferrocene ($Fc/g-C_3N_4$) under visible light, *Catal. Sci. Technol.*, 2023, **13**, 6297–6312.

96 X. X. Lu, Q. Li, S. H. Liu, R. Luo, H. Li, M. Zhang, C. P. Cui, G. P. Zhu, S. Chen and C. H. Liang, Fabrication of a novel $BiOI/KTaO_3$ p–n heterostructure with enhanced photocatalytic performance under visible-light irradiation, *RSC Adv.*, 2020, **10**(18), 10921–10931.

97 P. Vijayarengan, S. C. Panchangam, A. Stephen, G. Bernatsha, G. K. Murali, S. S. Loka, S. K. Manoharan, V. Vemula, R. R. Karri and G. Ravindran, Highly efficient visible light active iron oxide-based photocatalysts for both hydrogen production and dye degradation, *Sci. Rep.*, 2024, **14**(1), 12345.

98 Z. Yu, H. Moussa, M. Liu, R. Schneider, M. Moliere and H. Liao, Heterostructured metal oxides-ZnO nanorods films prepared by SPPS route for photodegradation applications, *Surf. Coat. Technol.*, 2019, **375**, 670–680.

99 Y. Zhu, Q. Xv, D. Wang, B. Sun, Y. Wang, Z. Han, Y. Gou, J. Liu and B. Li, Construction of a hollow $BiOI/TiO_2$/ZIF-8 heterojunction: enhanced photocatalytic performance for norfloxacin degradation and mechanistic insight, *J. Alloys Compd.*, 2022, **914**, 165326.

100 L. Zhi, S. Zhang, Y. Xu, J. Tu, M. Li, D. Hu and J. Liu, Controlled growth of AgI nanoparticles on hollow WO_3 hierarchical structures to act as Z-scheme photocatalyst for visible-light photocatalysis, *J. Colloid Interface Sci.*, 2020, **579**, 754–765.

101 M. Zhang, J. Qin, P. Yu, B. Zhang, M. Ma, X. Zhang and R. Liu, Facile synthesis of a ZnO–BiOI p–n nano-heterojunction with excellent visible-light photocatalytic activity, *Beilstein J. Nanotechnol.*, 2018, **9**, 789–800.

102 J. Liu, Q. Zhong, Y. Wang, Z. Zhang, H. Zheng, B. Yan and Y. Shi, Constructing AgI/BiSI p–n heterojunctions with an internal electric field for efficient degradation of refractory organic pollutants, *Arabian J. Chem.*, 2024, **17**(7), 105844.

103 G. Yan, K. Wang, Z. Jiang, K. Jiang, J. Peng and J. Xu, Flower-like ZnO/BiOI p–n heterojunction composites for enhanced photodegradation of formaldehyde and dyes, *J. Mater. Sci.: Mater. Electron.*, 2022, **33**(29), 23064–23074.

104 P. Y. Kuang, J. R. Ran, Z. Q. Liu, H. J. Wang, N. Li, Y. Z. Su, Y. G. Jin and S. Z. Qiao, Enhanced Photoelectrocatalytic Activity of BiOI Nanoplate–Zinc Oxide Nanorod p–n Heterojunction, *Chem. – Eur. J.*, 2015, **21**(43), 15360–15368.

105 S. Lei, C. Yang, H. Liao, J. Chen, J. Zhong and J. Li, Enhanced photocatalytic activity of N134 carbon black modified Bi_2WO_6 benefited from ample oxygen vacancies and boosted separation of photoexcited carriers, *Mater. Res. Bull.*, 2021, **133**, 111075.

106 P. G. R. Achary, P. Pattanaik and B. Nanda, Facile synthesis of lanthanum doped strontium manganite for photocatalytic decolourization of malachite green, *Inorg. Chem. Commun.*, 2023, **158**, 111545.

107 J. Low, J. Yu, M. Jaroniec, S. Wageh and A. A. Al-Ghamdi, Heterojunction photocatalysts, *Adv. Mater.*, 2017, **29**(20), 1601694.

108 X. Wang, C. Ding, H. Long, C. Peng, X. Xu, Y. Wu, Z. Yan, F. Jiang, R. Chang, S. Xue and W. Lv, Dye wastewater treatment through adsorption-photocatalysis using electroplating sludge-derived $NiFe_2O_4$@C catalyst, *Sep. Purif. Technol.*, 2025, **354**, 128894.

109 Y. Pan, F. Meng, J. Bai, B. Song and Q. Cao, Highly efficient peroxymonosulfate activation by $CoFe_2O_4$@ attapulgite–biochar composites: degradation properties and mechanism insights, *J. Environ. Chem. Eng.*, 2024, **12**(3), 112579.

110 M. K. Okla, B. Janani, S. Swetha, A. A. Alatar, I. A. Alaraidh, A. A. Al-ghamdi, R. F. Abdelaziz, M. A. Abdel-Maksoud, M. K. Rahiman and S. S. Khan, Environmental friendly nano-star CdS coupled ZnS on bi-polymer matrix: unravelling defects-rich nanoplatform for ultrahigh white light active direct S-scheme photodegradation of organic pollutants, *J. Alloys Compd.*, 2022, **925**, 166611.